International Geology Review

ISSN: (Print) (Online) Journal homepage: https://www.tandfonline.com/loi/tigr20

Miocene anatexis, cooling and exhumation in the Khumbu Himal, Nepal

Kyle P. Larson, John M. Cottle, Alfredo Camacho, Stephen Piercey & Djordje Grujic

To cite this article: Kyle P. Larson, John M. Cottle, Alfredo Camacho, Stephen Piercey & Djordje Grujic (2021): Miocene anatexis, cooling and exhumation in the Khumbu Himal, Nepal, International Geology Review, DOI: 10.1080/00206814.2021.1969524

To link to this article: https://doi.org/10.1080/00206814.2021.1969524

INTERNATIONAL GEOLOGY REVIEW
https://doi.org/10.1080/00206814.2021.1969524

Taylor & Francis
Taylor & Francis Group

Miocene anatexis, cooling and exhumation in the Khumbu Himal, Nepal

Kyle P. Larson[a], John M. Cottle[b], Alfredo Camacho[c], Stephen Piercey[d] and Djordje Grujic[e]

[a]Department of Earth, Environmental and Geographic Sciences, The University of British Columbia, Kelowna, BC Canada; [b]Department of Earth Science, University of California, Santa Barbara, CA, USA; [c]Department of Geological Sciences, University of Manitoba, Winnipeg, MB Canada; [d]Department of Earth Sciences, Memorial University, St. John's, NL Canada; [e]Department of Earth and Environmental Sciences, Dalhousie University, Halifax, NS Canada

ABSTRACT

The Khumbu region of Nepal is host to numerous large leucogranite bodies that comprise some of the most iconic peaks in the Himalaya. These leucogranites occur throughout the high-metamorphic grade rocks exposed there in the immediate footwall of the orogen-scale South Tibetan detachment system. Previous work on leucogranites in the area has been limited spatially but has yielded U-Th/Pb ages between ~23 and 16 Ma. The current study expands upon that work with 522 new individual zircon, monazite and xenotime U-Th/Pb analyses across 10 leucogranite specimens collected from across the Khumbu. The dates returned outline the episodic crystallization of leucogranites at ~19 and 17 Ma, both of which contain significant inherited age components presumably from their source rocks. $^{40}Ar/^{39}Ar$ dating of muscovite from the same leucogranite bodies indicate rapid cooling through Ar closure (~510 °C) on the scale of ~500 kyr. The weighted mean of all $^{40}Ar/^{39}Ar$ dates, 16.48 ± 0.05 Ma, coincides with the timing of motion along the normal-sense Qomolangma detachment indicating a potential genetic relationship between the leucogranite cooling and extension. Finally, U(-Th)/He dating of apatite and zircon show that cooling slowed significantly post argon closure and that the rapid cooling may have been ephemeral.

ARTICLE HISTORY
Received 23 February 2021
Accepted 14 August 2021

KEYWORDS
Humbu Himalaya; U(-Th)/Pb geochronology; $^{40}Ar/^{39}Ar$ thermochronology; U(-Th)/He thermochronology

1. Introduction

Anatexis is often a consequence of orogenesis and as such, it can serve as a record of the processes active during the development of collisional systems. Past researchers have linked the formation of anatextite to crustal differentiation (e.g. Sawyer 1994; Sawyer *et al.* 2011), a variety of mineral reactions (e.g. Harris and Inger 1992; Cottle *et al.* 2019; Dyck *et al.* 2020) and pressure-temperature (P-T) histories (e.g. Zhang *et al.* 2017; Phukon *et al.* 2019) that, when interpreted in the broader tectonic context, can be used to inform and even test models for orogenic system development (e.g. Annen *et al.* 2006; Groppo *et al.* 2012). In addition to serving as a marker of orogenic processes, the production, migration and accumulation of anatextite can also have a significant effect on rheology where even small volume percentages of melt can induce significant weakening of the crust (Beaumont *et al.* 2004). If sufficient melt can be retained within the rock, i.e. avoid being drained through compaction/shearing mechanisms (e.g. Scaillet and Searle 2006), the resultant rheological change can act as a feedback mechanism that influences the active deformational processes. As such, in large, hot orogenic systems, those with the potential to generate significant volumes of melt, understanding the spatial and temporal distribution of anatexite is a fundamental first-order baseline for understanding the evolution of the system.

The Himalaya is the modern-day type-example for continent-continent collisional systems. Previous work has characterized substantial volumes of Cenozoic anatexite along the length of the orogen from Pakistan in the west to Bhutan in the east (e.g. Schärer 1984; Schärer *et al.* 1986; Searle *et al.* 1989, 1997, 2010; Harrison *et al.* 1995; Searle 1999a; Lee *et al.* 2004; Zhang *et al.* 2004 and others; Streule *et al.* 2010; Visona *et al.* 2012; Gao *et al.* 2013; Lederer *et al.* 2013; Carosi *et al.* 2013; Zeiger *et al.* 2015; Faisal *et al.* 2016; Cottle *et al.* 2018, 2019; Fu *et al.* 2018; Hopkinson *et al.* 2020). These works, and many others, have outlined the interdependent history of metamorphism, anatexis and deformation during the evolution of the orogen.

CONTACT Kyle P. Larson kyle.larson@ubc.ca Department of Earth, Environmental and Geographic Sciences, The University of British Columbia, Okanagan, 3247 University Way, Kelowna, BC V1V 1V7, Canada

For submission to International Geology Review
Supplemental data for this article can be accessed here

Advances in analytical techniques in recent years now enable paired collection of both geochronological and geochemical data from laser ablation split stream (LASS) inductively coupled plasma mass spectrometry (ICP-MS) with laser spots approaching ~ 5 µm diameter and ~3 µm depth (Kylander-Clark 2017). This type of analysis has changed the scale at which studies are conducted both in the spatial and analytical sense. Whereas, in the recent past, detailed examination of the melt history of an area might involve 75–80 highly precise, but time consuming, isotope dilution thermal ionization mass spectrometry (ID-TIMS) U/Pb analyses from a few specimens (e.g. Viskupic *et al*. 2005), it is now possible to trade analytical precision for spatial precision and number of analyses. For example, a recent LASS-based investigation of the Manaslu pluton in west-central Nepal and a smaller, unnamed body in the Tama Kosi region of east-central Nepal comprised 1407 individual U-Th/Pb monazite spot analyses in 29 specimens and 337 combined U(-Th)/Pb monazite, zircon and xenotime spot analyses across 3 specimens, respectively (Cottle *et al*. 2018, 2019). This massive increase in the amount of material examined can provide a more complete picture of the characteristics of these melt systems. Moreover, the ability to directly tie mineral chemistry to time allows insight into the temporal evolution of magmatic systems, which can directly inform orogen-scale processes.

Herein we apply high-spatial resolution geochronology to re-examine the role of anatexis during orogenesis recorded in the Khumbu region of west-central Nepal (Figure 1). The region provides critical exposure of, and access to, different melt generations (e.g. Ferrara *et al*. 1983; Villa 1990; Pognante and Benna 1993; Weinberg and Searle 1999; Searle 1999a; Viskupic *et al*. 2005; Visona *et al*. 2012) at structural levels (close to the top of the exhumed, former metamorphic core) that can be significantly more difficult to access elsewhere along the mountain range. Characterizing the petrochronologic history of this iconic part of the Himalaya is an important step in better understanding the timescales of melting and its interrelationships with metamorphic and deformational processes.

2. Geological Background

The Nepalese Himalaya is characterized by laterally continuous belts of different lithotectonic affinity separated by large-scale north-dipping structures. From south to north these include the imbricated foreland basin deposits of the Siwaliks, which occupy the hanging wall of the Main Frontal thrust (Lavé and Avouac 2000). The top of the Siwaliks is marked by the Main Boundary thrust, which carries the low-to-medium metamorphic grade Lesser Himalayan sequence in its hanging wall (Gansser 1981; Seeber *et al*. 1981). The Lesser Himalayan sequence in Nepal consists dominantly of Proterozoic passive margin deposits (Martin *et al*. 2011) intercalated with various mid Proterozoic igneous rocks (Kohn *et al*. 2010; Larson *et al*. 2019). Both the Lesser Himalayan sequence and the structurally overlying Greater Himalayan sequence, which comprises late Proterozoic to Palaeozoic continental margin sediments (Parrish and Hodges 1996) and orthogneiss (Godin *et al*. 2001), preserve an apparent inverted metamorphic field gradient with metamorphic conditions generally increasing structurally upward (Arita 1983; Pêcher 1989; Searle and Rex 1989). This apparent inverse metamorphic field gradient includes the Main Central thrust, which marks the boundary between the two lithotectonic units (Gansser 1964; Searle *et al*. 2008; Martin 2017). Metamorphism in the Greater Himalayan sequence typically ranges from staurolite or kyanite-bearing schists at lower structural levels to sillimanite and K-feldspar-bearing migmatites and massive leucogranite plutons at the highest structural levels (Kohn 2014; Waters 2019). The South Tibetan detachment system delineates the upper boundary of the Greater Himalayan sequence (Kellett *et al*. 2019). It comprises a series of down-to-the-north extensional structures that can be mapped along almost the entire orogen that were at least partially coeval with movement along the Main Central thrust (Godin *et al*. 2006). The South Tibetan detachment system places low metamorphic grade to unmetamorphosed sedimentary rocks of the Tethyan sedimentary sequence adjacent to the high-metamorphic grade rocks of the Greater Himalayan sequence (Cottle *et al*. 2007).

The geology of study area examined herein, the Khumbu region of Nepal (Figure 1), contains migmatitic orthogneiss and sillimanite-bearing paragneiss and leucogranite of uppermost portion of the Greater Himalayan sequence (Pognante and Benna 1993; Searle *et al*. 2003). Those rocks are juxtaposed, in peaks of Cho Oyu, Mt. Everest, Lhotse, and others against Tethyan sedimentary sequence rocks by the South Tibetan detachment system (Figure 1; Searle 1999b).

Geological research in the Khumbu region has a long history. Much of the early work focused around Mt. Everest in collaboration with climbing expeditions (Heron 1922; Odell 1925; Wager 1933). More traditional geological investigation in the Khumbu followed with detailed reports of geological units, preliminary metamorphic pressure-temperature (P-T) estimates and radiogenic dating (e.g. Bordet 1961; Ferrara *et al*. 1983; Brunel and Kienast 1986; Lombardo *et al*. 1993). This early work helped set the context for later studies that

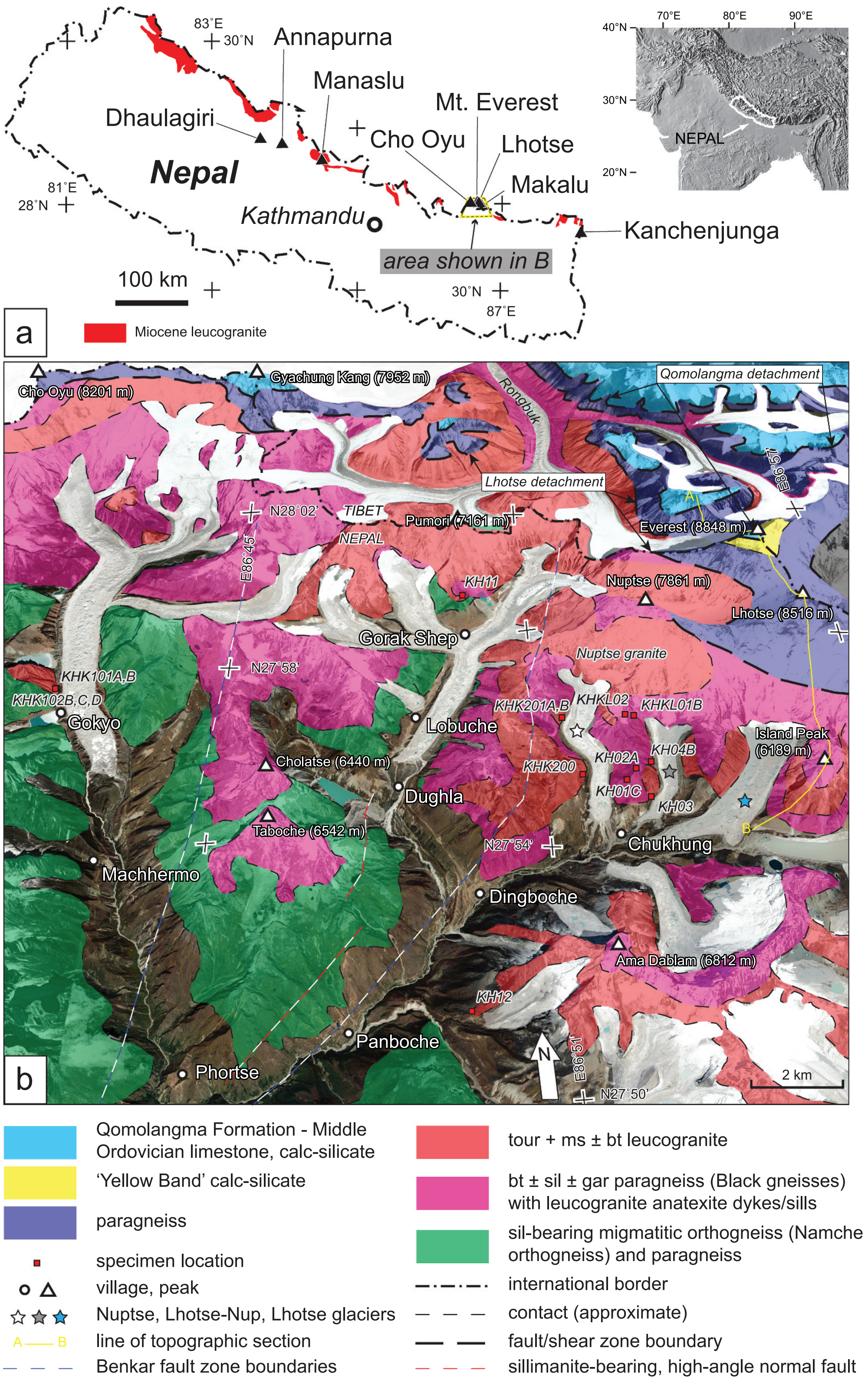

Figure 1. A) General location map showing the political boundary of Nepal with >8000 m peaks located. The present study area is marked by a yellow and black dashed trapezoid. Leucogranite locations after Pearson and DeCelles (2005). Regional digital elevation map after Searle *et al*. (2008). B) Isometric view of the study area with geology drawn from (Pertusati et al., pers. comm; Weinberg and Searle 1999; Carosi *et al*. 1999a, 1999b; Searle 1999a, 1999b; Searle *et al*. 2003; Hubbard *et al*. 2021). Background image from Google Earth with data ©2021 CNES/Airbus, ©2021 Maxar Technologies.

reported further detailed metamorphic P-T conditions (Hubbard 1989; Searle *et al*. 2003; Jessup *et al*. 2008), and timing and duration of melting (Schärer 1984; Villa 1990; Simpson *et al*. 2000; Catlos *et al*. 2002; Viskupic *et al*. 2005; Cottle *et al*. 2009, 2015; Streule *et al*. 2010). Collectively, these studies have outlined a complex geological history comprising early metamorphism during late Eocene time reaching peak conditions of ~625–725 °C and ~3–7 kbar in the early Miocene epoch. Temperatures are generally lower and pressures generally higher at lower structural levels with the inverse characteristic for rocks at higher structural levels, which also host abundant leucogranite anatextite (Searle *et al*. 2003).

The timing, duration, process of anatexis and melt emplacement mechanisms of plutons in the Khumbu and adjacent parts of Tibet have all been reported on in a variety of works (e.g. Searle 1999a; Simpson *et al*. 2000; Viskupic *et al*. 2005; Cottle *et al*. 2009, 2015; Visona *et al*. 2012; Schultz *et al*. 2017) that, together, outline a melt crystallization history with broad peaks at ca. 16, 21 and 23 Ma (n = 41 specimens) (Figure 2). The generation of melts in the Khumbu and environs has been attributed to either fluid present or fluid absent partial melting of muscovite and/or biotite bearing metasedimentary rocks during heating and/or decompression (Searle 1999a; Groppo *et al*. 2012; Visona *et al*. 2012). Emplacement of km-scale leucogranite bodies in the region has been explained through injection via giant feeder sill and dyke networks (Searle 1999a), whereas smaller scale dykes have been interpreted to reflect fluid assisted brittle-ductile shearing along discrete structures (Musumeci 2002).

The present study builds upon previous work and employs new methodologies (outlined below) to not only quantify the spatial and temporal distribution of melt in the Khumbu, but also enable further insight into 1) the longevity of individual bodies and the mode of pluton assembly – discrete pulse versus protracted melting through examination of the dates extracted from the bodies, 2) potential correlation of spatially disparate magmatic bodies based on geochronology and geochemistry, and 3) timing of emplacement/crystallization/cooling with respect to large-scale, first-order orogenic structures through comparison the data presented herein and previously published data.

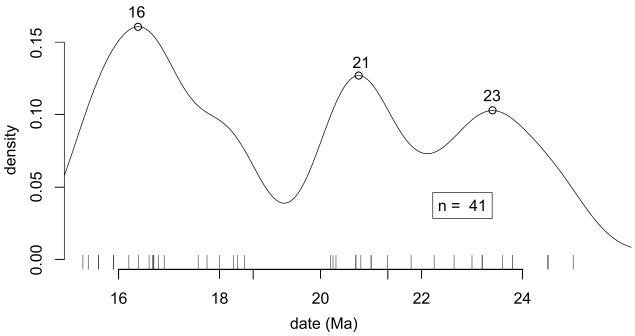

Figure 2. Kernel density estimation of previously published leucogranite dates from the Khumbu region. Data are from Searle (1999a), Simpson *et al.* (2000), Viskupic *et al.* (2005), Cottle *et al.* (2009), (2015)), Visona *et al.* (2012) and Schultz *et al.* (2017)

3. Methods

A suite of specimens was collected from the Khumbu region (Figure 1) during fieldwork arranged with the support of the Department of Geology, Tri-Chandra College and the Department of Mines and Geology, Government of Nepal. The sampling location coordinates are included in Supp. Table 1. The results of whole rock geochemistry, U(-Th)/Pb zircon, monazite and xenotime geochronology, ^{40}Ar/^{39}Ar thermochronology, and U-Th-He thermochronology from subsets of the suite collected are presented in the following sections.

3.1. *Whole rock geochemistry*

Rock specimens selected for whole rock geochemistry were analysed in two batches using two different methods (data available in Supp.Table 2). Specimens KH02A, KH03, KH11 and KH12 were crushed, powdered, and fused into glass beads at the University of California, Santa Barbara. Major element analysis of those beads was carried out via X-ray fluorescence (XRF) at Pomona College at Pomona, California using a PanAnalytical Axios wave-length dispersive instrument. Calibration and specimen measurement protocols were modelled after those employed by the Washington State University Geoanalytical Laboratory (Johnson *et al*. 1999). Pieces of the beads used for XRF analyses were flaked off, embedded in epoxy, polished and analysed for trace element compositions via laser ablation ICP-MS. A Photon Machines Analyte excimer laser source was used with a 100 µm spot to introduce specimen material from the glass bead into a Agilent 8900 triple quadrupole ICP-MS housed in the Fipke Laboratory for Trace Element Research at the University of British Columbia, Okanagan. Glass reference materials NIST610 (primary) and NIST612 (secondary) were measured throughout the analytical session. Trace element concentrations of unknowns were reduced using Iolite v.4 (Paton *et al*. 2010) with Si used as the internal elemental standard. Elemental abundances are within 10% of accepted values for

NIST610 (GeoReM database, application version 27, http://georem.mpch-mainz.gwdg.de) (Jochum *et al.* 2005).

Specimens KHK100C, 101A, 101B, 102B, 102 C, 102D, 200, 201A and 201B were analysed for whole rock and trace element abundances at the Saskatchewan Research Council. Specimens were crushed and powdered in an agate mill following standard procedures before lithium borate fusion and analysis by both ICP-MS (trace elements) and ICP-OES (major elements).

3.2. U(-Th)/Pb Geochronology

Zircon, monazite and xenotime grains were separated from nine specimens via standard crushing and heavy mineral separation techniques. These specimens were analysed for U, Th, and Pb isotopes at the University of California, Santa Barbara across multiple analytical sessions following the methods outlined in Kylander-Clark *et al.* (2013) with modifications presented in McKinney *et al.* (2015). The data are available in Supp.Table 3.

Monazite from specimens KHKL01B and KH02A were analysed with an 8 micron spot using monazite 44069 (426 ± 3 Ma; Aleinikoff *et al.* 2006) as the primary reference material. Repeat analyses of the secondary reference material 'Stern' returned a ^{207}Pb corrected ^{206}Pb/^{238}U age of 507.0 ± 2.6 (MSWD = 0.7, n = 26/26) and a ^{208}Pb/^{232}Th age of 505.1 ± 3.2 (MSWD = 0.8 n = 23/26). Those dates compare with expected ages of 507.8 ± 1 Ma or 511.9 ± 1.5 Ma for the ^{206}Pb/^{238}U system (Kylander-Clark *et al.* 2013; Horstwood *et al.* 2016) and 496.6 ± 1.6 Ma for the ^{208}Pb/^{232}Th system (Kylander-Clark *et al.* 2013), well within the 2% typical reproducibility of the method.

Monazite and xenotime from specimens KHK200, 102B, 201B, 201A were analysed in a single analytical session; monazite 44069 was used as the primary reference material. Twenty-one repeat analyses of Stern reference material yielded a ^{207}Pb corrected ^{206}Pb/^{238}U age of 515 ± 3 Ma (MSWD = 5, n = 21/21), while 19 of 21 analyses define a ^{208}Pb/^{232}Th age of 493 ± 3 Ma (MSWD = 1.71). Those ages overlap with the age expected as outlined above. In addition, monazite 'FC1' was also analysed yielding a ^{207}Pb corrected ^{206}Pb/^{238}U age of 58.0 ± 0.4 Ma (MSWD = 2.31, n = 10/11) and a ^{208}Pb/^{232}Th age of 56.8 ± 0.9 Ma (MSWD = 1.3, n = 11/11). Those ages are in general agreement with expected ^{206}Pb/^{238}U ages of 55.6 ± 0.3 to 56.2 ± 0.2 Ma (Horstwood *et al.* 2003; Kylander-Clark *et al.* 2013) and a ^{208}Pb/^{232}Th age of 54.3 ± 0.2 Ma (Kylander-Clark *et al.* 2013).

Zircon were analysed in two different sessions. The first, which included KH03, KH11 and KH12 was run with a spot size of 10 microns using the '91500' reference zircon for primary calibration and 'GJ-1' as the secondary reference zircon. Twenty-four repeat analyses of GJ-1 yielded a ^{207}Pb-corrected ^{206}Pb/^{238}U age of 606 ± 2 (MSWD = 0.6). Specimens KHK201A, KHK201B and KHK 101B were analysed in the second session. As before, 91500 was used as the primary reference material with GJ-1 as the secondary. Forty-one analyses of GJ-1 outline a ^{207}Pb-corrected ^{206}Pb/^{238}U age of 601 ± 3 Ma (MSWD = 0.3, n = 41/41). The secondary analyses from both analytical sessions are within 2% of the accepted age.

When collected, trace element data for the minerals was analysed from the same analytical spot/ablated volume as the age information via the 'split stream' approach as outlined in Kylander-Clark *et al.* (2013). Typical trace element reproducibility following this method is 3–5% Cottle et al. (2019).

Monazite dates reported in this contribution are based on the ^{208}Pb/^{232}Th system to avoid potential complications of excess ^{206}Pb from unsupported ^{230}Th (Schärer 1984). All zircon and xenotime dates reported are derived from ^{207}Pb-corrected ^{206}Pb/^{238}U ratios. Data was not filtered for discordance prior to plotting. All dates are reported at two standard errors (SE).

3.3. ^{40}Ar/^{39}Ar Geochronology

Muscovite and biotite mica were hand-picked directly from hand specimens or from post-crushing separates during processing of specimens for U-Th-Pb geochronology. Care was taken to select optically pristine crystals, free of inclusions. After irradiation, single crystals from each specimen were irradiated analysed at the University of Manitoba using laser step heating as outlined in Brubacher *et al.* (2020). Uncertainties associated with ^{40}Ar/^{39}Ar dates in the text and figures are reported at 2SE, while individual steps in the table are shown at 1SE. The full dataset is available in Supp.Table 4.

3.4. U-(Th)/He Geochronology

Apatites and zircons for (U-Th)/He analyses were manually selected under high-magnification stereoscopic microscope. Preference was given to the euhedral, transparent, inclusion- and cracks-free grains with a smallest dimension being not less than 70 m (Supp. Figures S1, S2). All selected grains were packed in Nb tubes. Before packing grains were measured and photographed. These measurements were used to calculate an α-ejection correction (Farley *et al.* 1996).

Helium measurements were completed at Dalhousie University on an in-house built He extraction line equipped with 45 W diode laser and Pfeiffer

Vacuum Prisma quadrupole mass-spectrometer. Each Nb packet was heated using a laser to release He. Apatites were heated to 1050°C for 5 minutes, whereas zircons were heated to 1250°C for 15 minutes. After He extraction a precisely measured aliquot of ^{3}He was added to the sample and ^{3}He/^{4}He ratio was measured using quadrupole mass-spectrometer. This procedure was repeated once for apatites to make sure no He is left in the grain. Since zircon retains He better than apatite, He extraction was repeated up to 3–4 or more times until the amount of He in the last re-extraction was less than 1% of total He extracted from this grain. Typical errors are in the range of 1.5–2% (1σ) for both zircons and apatites. Samples were analysed in groups of 36, each group included 2 Durango apatite standards for apatite analyses, or 2 Fish Canyon tuff zircon standards in case of zircon analyses. These standards went through the same analytical procedures as unknown samples to ensure accuracy, reproducibility, and reliability of the data. Eighty-five analyses of the Durango apatite (32.0 ± 1 Ma; Farley 2002) yielded a date of 31.4 ± 1.8 Ma (σ), while 83 analyses of Fish Canyon tuff zircon (28.3 ± 2.6 Ma; Reiners 2005), gave an age of 28.1 ± 1.9 Ma (1σ).

After He extraction, both apatites and zircons were dissolved following standard dissolution protocol for these minerals. Apatite grains were dissolved in 7 N HNO_3 at 80°C for 1.5 hour, whereas zircon grains were dissolved in high-pressure dissolution vessels in mixture of concentrated HF and HNO3 at 200°C for 96 hours. Prior to dissolution all samples were spiked with a mixed ^{235}U, ^{230}Th, and ^{149}Sm spike. Isotopic ratios were measured using iCAP Q ICP-MS.

All raw data were reduced using the Helios software package developed by R. Kislitsyn and D. Stockli specifically for (U-Th)/He data reduction. α-ejection correction was calculated based on surface to volume ratio (Farley *et al*. 1996). Final data are presented in Supp. Table 5.

4. Results

4.1. Overview of Specimens

A total of 13 specimens collected from across the Khumbu region of Nepal (Figure 1) were analysed using the U-Th-Pb, ^{40}Ar/^{39}Ar and/or U-Th-He methods. Ten of the plutonic specimens are granite while one, KHK102D, is a granodiorite (Supp. Figure 3); specimens KH01C and KH04B are meta-pelite.

All but one of the plutonic specimens collected have no apparent discernible evidence of deformation (see KHK102B below). Moreover, none of the outcrops investigated contained any deformation that could be attributed to the movement along any single structure. The specimens can be broadly separated into two categories. Specimens KH03, KH11, KH12 and KHK101B preserve a generally equigranular two mica-assemblage of quartz + plagioclase + muscovite + K-feldspar + tourmaline + biotite with accessory zircon (Supp. Figures 4, 5). A key feature of these granites, which differentiates them from the others, is the presence of cm-scale skeletal tourmaline (Figure 3A, Supp. Figures 4, 5). Searle *et al*. (2003; their Figure 6) noted the occurrence of the same tourmaline 'ghosts' in leucogranite at Ama Dablam (similar to KH12) and above Everest base camp (Figure 1).

Specimens KHKL01B, KHK200, KHK201A and KHK201B were all collected from outcrops interpreted to be associated with the Nuptse granite (Figure 3B). The specimens contain the equigranular mineral assemblage of quartz + plagioclase + muscovite + K-feldspar + tourmaline and accessory monazite ± zircon ± xenotime (Supp. Figure 6). Biotite is observed occasionally in specimen KHK200, while KHK201A records locally pervasive muscovite alteration of plagioclase.

Specimens KHK102B, C and D were collected north of the village of Gokyo in the northwest part of the Khumbu (Figure 1), from one of the outcrops examined in detail by Viskupic *et al*. (2005; their Figure 2). KHK102B is equivalent to their specimen 00SK09 and KHK102C is equivalent to their 00SK10. Specimen KHK102B is from a sill, parallel to the main foliation in outcrop, and appears to be partially boudinaged (Figure 4A), but is little deformed in thin section (Supp. Figure 5). Moreover, the sill morphologies, including a bulbous protrusion along the top (Figure 4A) and apparent interfingering within the 'neck zone' (Figure 4B), are consistent with primary intrusive structures (Bons *et al*. 2004). It is possible that KHK102B represents a finger-style intrusion (Pollard *et al*. 1975; Spacapan *et al*. 2017). The mineral assemblage in KHK102B is quartz + plagioclase + muscovite + tourmaline + K-feldspar (Supp. Figure 5) with accessory xenotime + monazite ± zircon. Specimen KHK102D is a thin sill also parallel to the main foliation (Figure 4C). It is granodioritic in composition (Supp. Figure 3), significantly more melanocratic than the other specimens collected as part of this study, with dominant plagioclase + quartz + biotite with no apparent tourmaline or muscovite (Supp. Figure 5). The dyke associated with specimen KHK102C, a quartz + K-feldspar + plagioclase + muscovite + biotite granite, cuts across the foliation (Figure 4A, C) and KHK102D, and thus is the youngest phase sampled in the outcrop.

Specimen KH02A was collected from an undeformed granite dyke that crosscuts the main foliation just north of the village of Chukhung (Figure 1, Supp. Figure 7B). It

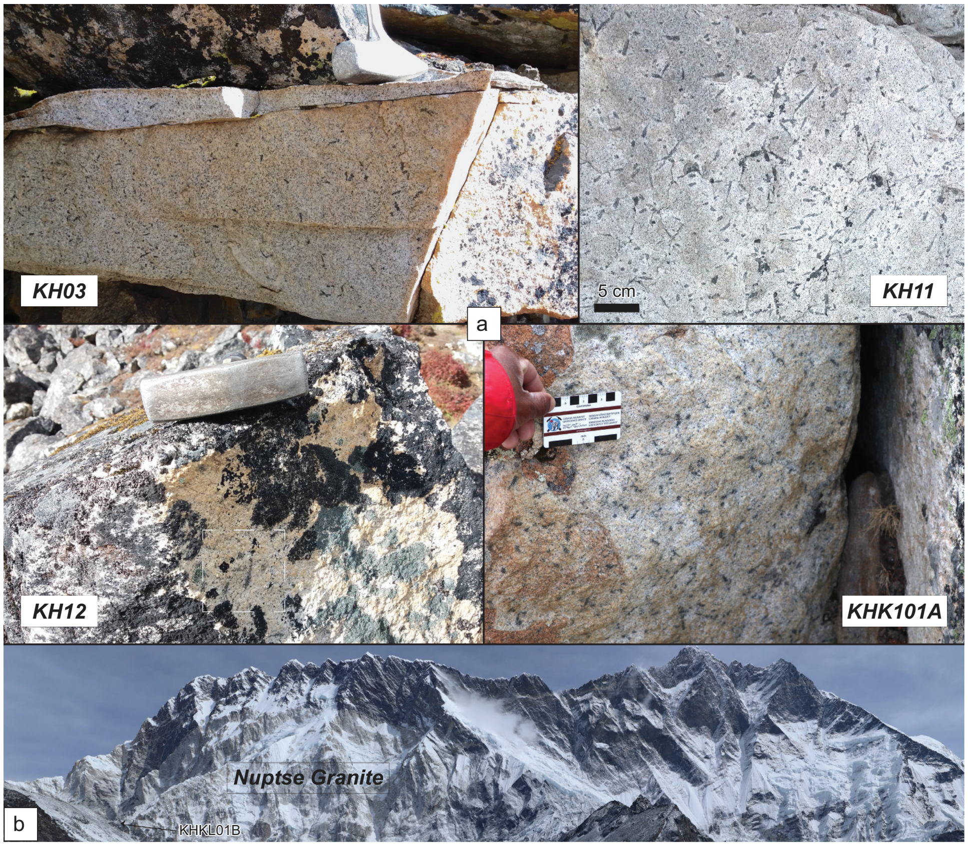

Figure 3. A) Field photographs of cm-scale, skeletal tourmaline bearing leucogranite rocks. Hammer head is approximately 15 cm long. B) Panorama photograph looking north at the Lhotse/Nuptse wall showing the Nuptse leucogranite (labelled) and the sampling location for specimen KHKL01B.

contains the assemblage of quartz + K-feldspar + plagioclase + muscovite + tourmaline (Supp. Figure 4A) with accessory monazite and locally contains xenoliths of the country rock. Localized alteration of feldspar is evident in thin section. The country rock it cuts, KH01C, contains a well-developed foliation marked by biotite and muscovite laths separating thin quartz ± plagioclase aggregates (Supp. Figure 7C). Similar mineralogy is observed in specimen KH04B collected farther north along the Chukhung ridge (Supp. Figure 7D). In that specimen aligned muscovite + biotite intergrowths also mark the main foliation and separate equigranular quartz and feldspar-rich aggregates.

4.2. *Whole rock geochemistry*

Major, trace, and rare earth elements were used to classify and evaluate the geochemical characteristics of the plutonic rocks. With the exception of KHK102D, which has intermediate SiO_2 content, all specimens have elevated SiO_2 (>70 wt%) (Figure 5A), which makes classification difficult (e.g. Frost *et al.* 2001). Eleven of the specimens cluster at high K_2O and low Na_2O (>4 and >3 wt %, respectively) with two specimens containing elevated Na_2O and lower K_2O (KHK102B; KHK102D; Figure 5B). In total alkalis versus silica space (Figure 5C) most specimens occupy the alkali granite/subalkalic granite fields while KHK102D has an alkalic syeno-diorite affinity. Further separation between specimens is apparent in Nb/Y-Zr/Y space, where specimens KHK102D, KHK200, KHK201A, B have a Nb/Y < 0.7 (subalkaline) (Winchester and Floyd 1977) and a generally lower (<5) Zr/Y relative to the other specimens (Figure 5D). All specimens plot proximal to the upper crustal line in upper crust normalized La-Sm space (Figure 5E).

N-MORB normalized multi-element plots are illustrated in Figure 5G. KHK102D, the low SiO_2 specimen, has a light REE (LREE)-enriched pattern (high La/Yb) with distinctive negative Nb and Ti anomalies, common of rocks derived from upper crustal sources (e.g. calc-alkalic-like crust) (Figure 5G). Most other specimens have patterns indicative of moderate LREE-enriched patterns with negative Nb and Ti anomalies (Figure 5G). The features present in these rocks are similar to those from rocks derived or partly influenced by continental crust/continental arc crust and are partly echoed by the Ta-Yb systematics of the rocks, where most rocks cluster within and around the syn-

Figure 4. A) Photograph (view-to-the-west) of the outcrop from which KHK102B, KHK102C and KHK102D were sampled showing their field relationships. The same outcrop was photographed and investigated in Viskupic *et al.* (2005). B) Close-up photograph of the location from which KHK102B was collected. The outcrop location is shown in A. C) Crosscutting relationships between KHK102C and KHK102D. Outcrop is shown in A.

collisional granite field, with one occurring within the volcanic arc granite field (Figure 5F). Given the leucogranitic nature of these materials and their setting, these tectonomagmatic discrimination signatures are not surprising.

Zirconium concentrations in the specimens that yielded zircon for U/Pb dating (see below) range between 36 and 76 ppm (Supp. Table 2). Those concentrations correspond to zirconium saturation temperatures between 690 °C and 753 °C (Watson and Harrison 1983; Hanchar and Watson 2003).

4.3. U-Th/Pb Geochronology

Eleven specimens were analysed for U(-Th)/Pb geochronology, 6 of which yielded zircon separates, 7 contained monazite separates and 3 yielded xenotime. Those that yielded only zircon (see below) tend to be more alkaline (Figure 5D) than those that contain monazite. Two specimens, KHK102C and KHK102D, that were processed for mineral separation did not yield any datable material.

Zircon grains from specimens KH03, KH11, KH12, KHK101B, KHK201A and KHK201B are commonly characterized by prismatic shapes. Under cathodoluminescence, grains have variably dark or bright, rounded cores, either bright well-zoned mantles or darker metamict mantles and typically medium to dark rims (Supp. Figure 8). Zircon rims were generally targeted for spot analyses (Supp. Figure 8) in an effort to avoid complication from inherited material common in these leucogranite (e.g. Copeland *et al.* 1988; Harrison *et al.* 1995). Grain interiors were not entirely avoided, however, to ensure representation of different age components.

Analysis of 138 zircon grains across all specimens yielded 334 ^{207}Pb-corrected ^{206}Pb/^{238}U dates that range in age from Paleoproterzoic to Cenozoic (Supp. Table 1) with dominant middle Miocene and Early Ordovician populations (Figure 6A). Because the focus of this study is on Himalayan anatexis we will restrict our discussion to <60 Ma dates (Figure 7). Two hundred and twenty-two <60 Ma dates comprise two main peaks, one at 24 Ma and a second at 17 Ma (Figure 6B). The young population is dominated by results from specimens KH03, KH11, KH12 and KHK101B (Figure 8), whereas the late Oligocene age population is broadly contributed to from nearly all specimens.

Titanium concentrations were measured with age information in specimens KHK101B, KHK201A and KHK201B. Titanium in zircon thermometry (e.g. Ferry and Watson 2007) from KHK201A yields an average temperature of 624 ± 32 °C, in grains from KHK201B Ti

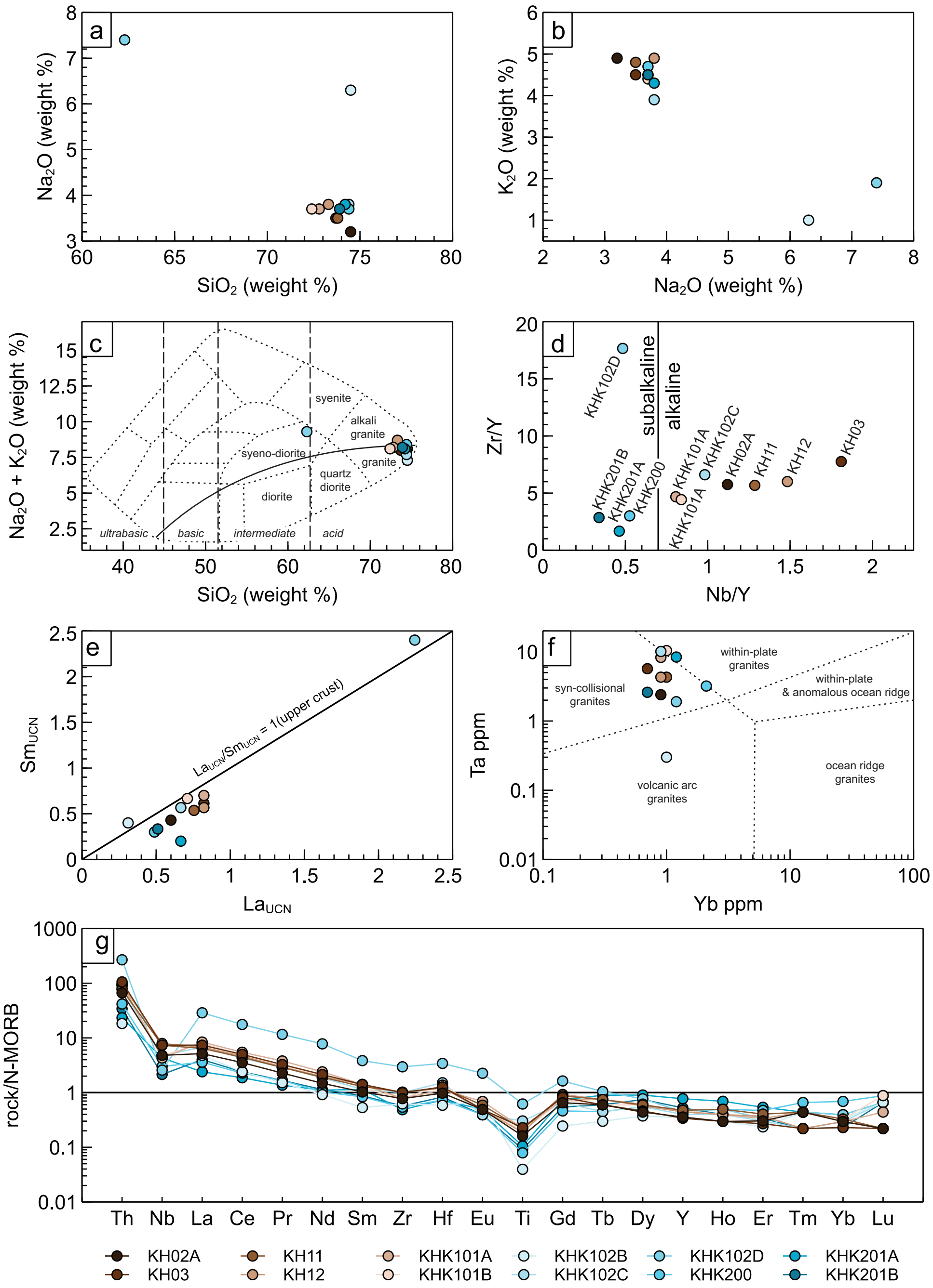

Figure 5. Geochemical data shown in various plots. See D and G for symbol legends. A) Na_2O vs SiO_2 – see text for discussion. Symbols are defined in parts D and G. B) Na_2O vs SiO_2 – see text for discussion. C) Total alkalis versus SiO_2 diagram of .Cox *et al.* (1979). D) Nb/Y-Zr/Y plot with alkalinity boundaries as per Winchester and Floyd (1977). E) Upper crust normalized La-Sm plot. Upper crustal values from McLennan (2001). F) Ta-Yb granite discrimination diagram from Pearce *et al.* (1984). G) N-MORB normalized multi-element plot. Values from Sun and McDonough (1989)

concentrations define an average temperature of 645 ± 8 °C and finally in KHK101B zircon, Ti indicates an average temperature of 710 ± 4 °C.

Monazite dates from grain separates of KH02A, KHK100C, KHK102B, KHK200, KHK201A, KHK201B, KHKL01B (Supp. Figure 9) are dominantly Cenozoic with only two of the 247 dates returned being >60 Ma. Spot analyses were located to obtain representative analyses from the different chemical zones identified in element maps (Supp. Figure 9). The monazite $^{208}Pb/^{232}Th$ ages are generally between ~30 and 17 Ma (Figure 10) with a significant peak ca. 25 Ma and less well-defined peak ca. 19 Ma (Figure 6C). The record of these two populations is variable across the specimens analysed (Figure 11) with most specimens contributing dominantly to

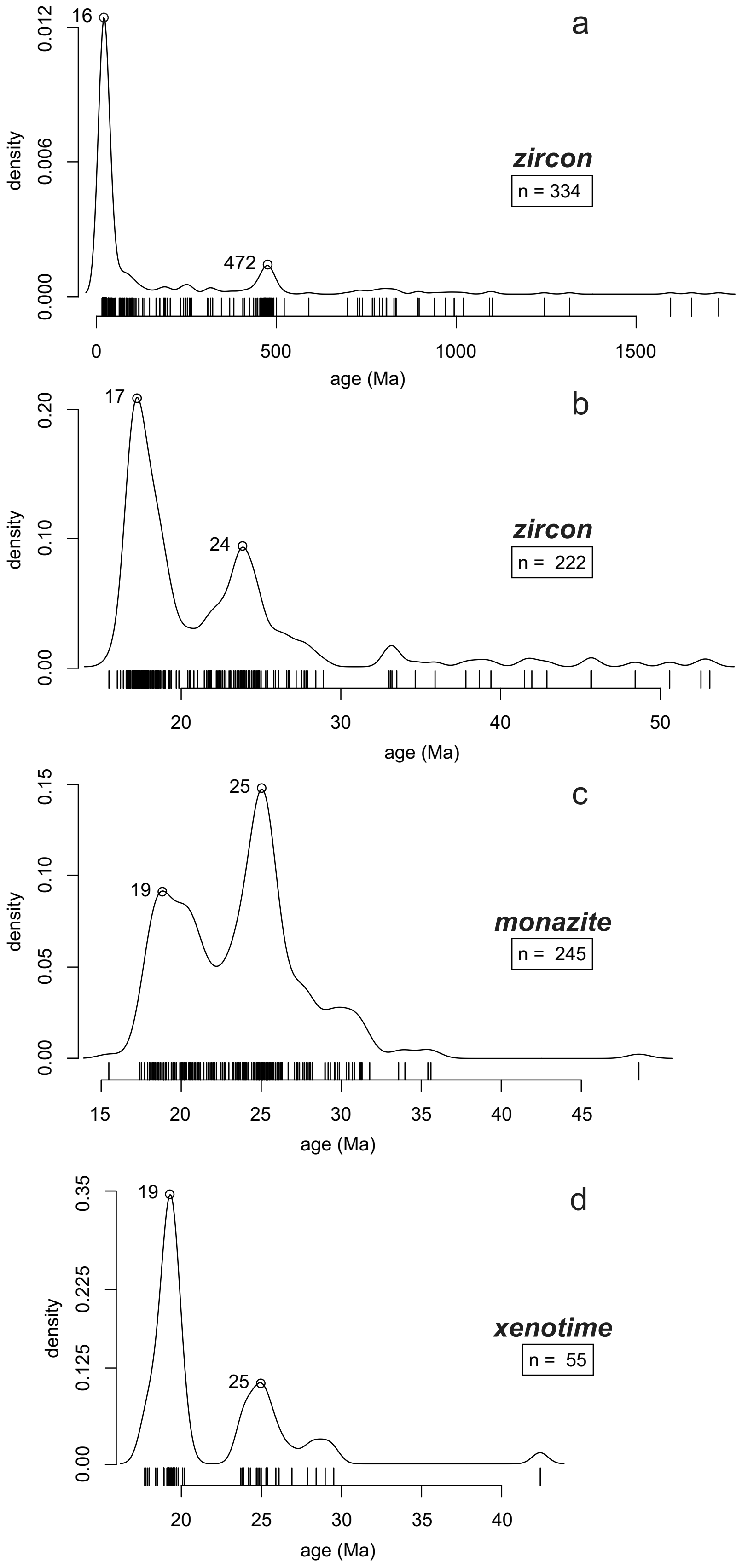

Figure 6. Kernel density estimation plots of the new data from the present study. A) ^{207}Pb corrected (following Stacey and Kramers 1975) ^{206}Pb/^{238}U zircon dates analysed. B) ^{207}Pb corrected ^{206}Pb/^{238}U zircon dates restricted to those <55 Ma. C) ^{208}Pb/^{232}Th monazite dates from this study. D) ^{207}Pb corrected ^{206}Pb/^{238}U xenotime dates from this study.

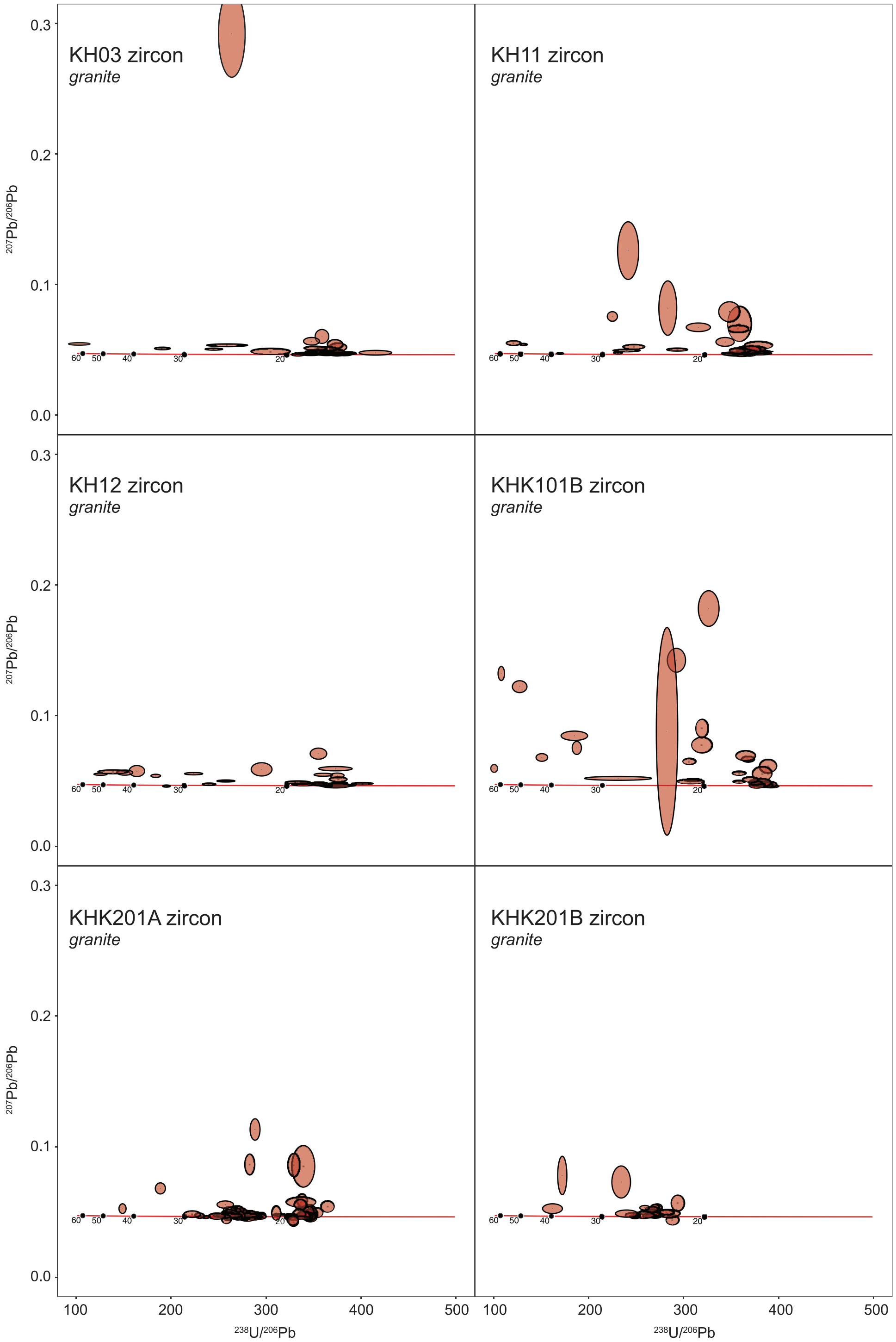

Figure 7. ^{207}Pb/^{206}Pb versus ^{238}U/ ^{206}Pb Tera-Wasserburg concordia plots of zircon analyses from this study. Only the Cenozoic data are shown. Specimens as marked. Plots generated using the ChrontouR package for the open R platform (Larson 2020).

one population. Specimen KHK201A is the exemption as it records well-defined ca. 25 and 19 Ma monazite sub-populations (Figure 11).

Monazite trace element data from KHK200, 201A and 201B show consistent trends across specimens in which the Gd/Lu ratio increases with younger age. This pattern is driven mainly by decreasing HREE through time (Supp. Figure 10). In addition, while there is a pronounced negative Eu anomaly across nearly all specimens, KHK201A and B show a decrease in the anomaly with younger ages (Supp. Figure 10).

Analysis of xenotime from KHK102B, 200 and 201B (Supp. Figure 9) yields only Cenozoic ages with 55 of 56 dates being <60 Ma (Figure 7D). Those dates outline

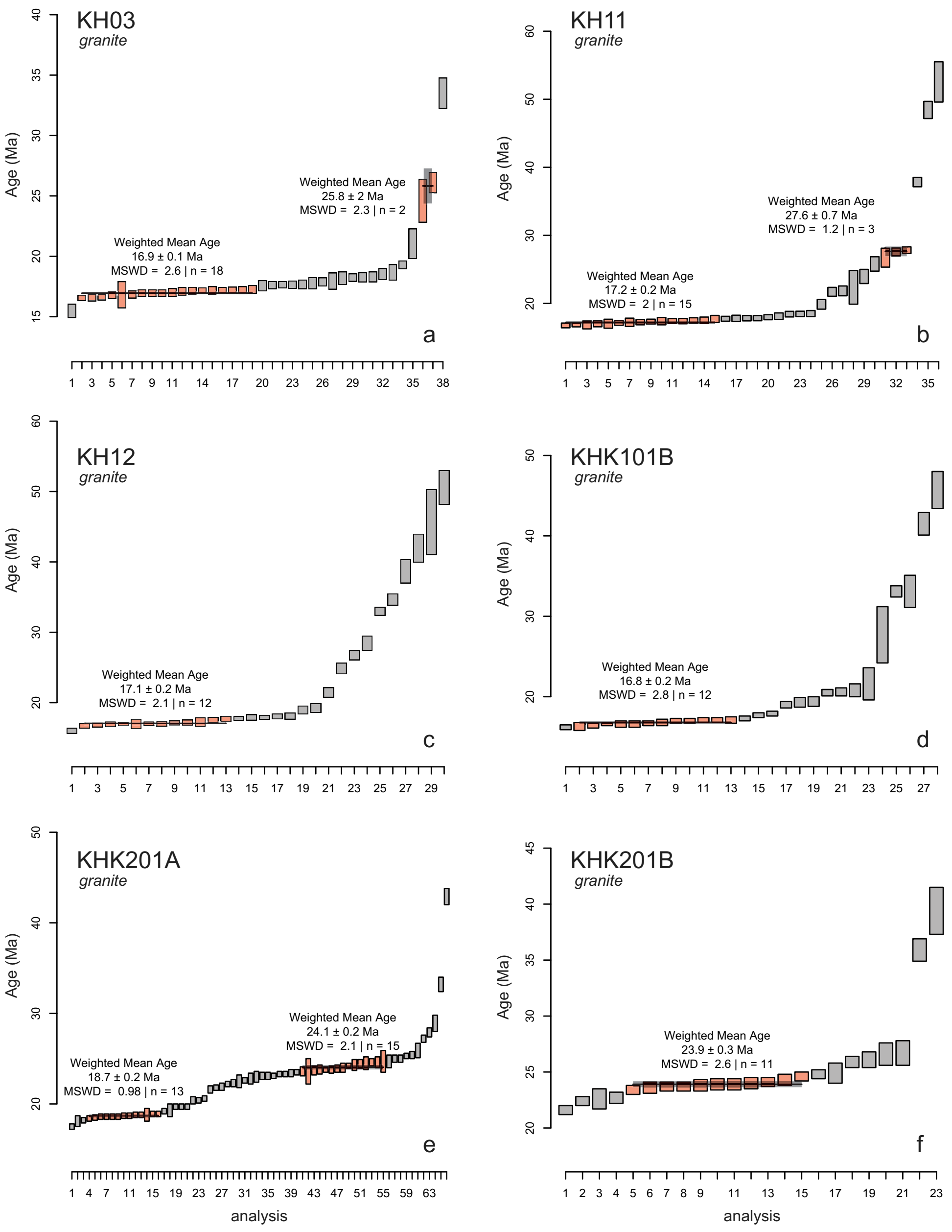

Figure 8. ^{207}Pb corrected (following Stacey and Kramers 1975) ^{206}Pb/^{238}U zircon dates with weighted mean ages identifiable populations indicated. Plots generated using the ChrontouR package for the open R platform (Larson 2020).

two main sub-populations (Figure 12) with the same age as those defined by monazite; ca. 25 and 19 Ma. Similar populations are delineated by ^{207}Pb-corrected ^{206}Pb/^{238}U weighted mean ages in specimens KHK102B and 200.

Trace element data collected with isotopic age data in xenotime record decreasing HREE concentrations with younger ages (Supp. Figure 10B). Furthermore, KHK102B shows an increase in negative Eu anomaly with younger ages, whereas this is not apparent in KHK200 (Supp. Figure 10B).

4.4. ^{40}Ar/^{39}Ar Geochronology

Seven specimens from across the Khumbu were analysed by the ^{40}Ar/^{39}Ar method producing seven muscovite and two biotite dates. All ^{40}Ar/^{39}Ar dates quoted below are reported at 2SE (see Supp. Table 2 for full analytical data).

Specimens KH01C and KH04B are muscovite bearing schist and paragneiss, respectively, collected from the same ridge north of Chukhung (Figure 1). Single grain step-heating analyses from these specimens yield indistinguishable plateau ages of 16.6 ± 0.1 Ma (KH01C) and

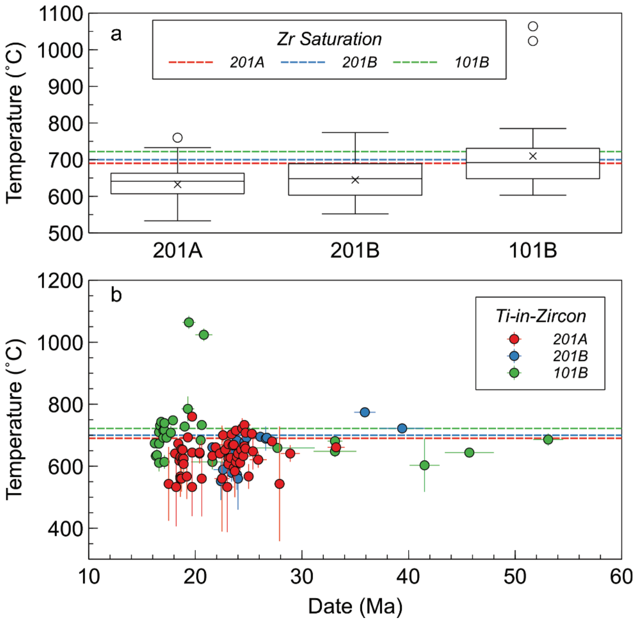

Figure 9. A) Titanium-in-zircon temperature whisker plots for specimens KHK201A, KHK201B and KHK101B. Temperature calculated from zirconium saturation (e.g. Hanchar and Watson 2003) is also shown. B) Titanium-in-zircon temperatures for each <60 Ma laser spot analysis for the same specimens as in A.

16.8 ± 0.3 (KH04B) Ma (Figure 13). The remaining specimens analysed, KH11, KH12, KHK101A, KHK200 and KHK201A are all undeformed muscovite + tourmaline ± biotite bearing granites. All five specimens yield nearly indistinguishable muscovite ages ranging between 16.4 ± 0.1 Ma and 16.9 ± 0.1 Ma (Figure 13).

The biotite date measured in KHK101A, 17.0 ± 0.1 Ma, is within uncertainty of the muscovite date, 16.6 ± 0.5 Ma from the same specimen (Figure 13). Similarly, the biotite date returned from KHK200, 16.4 ± 0.1 Ma, overlaps with the muscovite age from that specimen, 16.5 ± 0.1 Ma (Figure 13).

4.5. *U(-Th)/He Geochronology*

Four specimens (KH03, KH12, KHKL01B; KHK201A) were targeted for zircon U-(Th)-He analyses. Apatite separated from three of those same four specimens (KH03, KHKL01B, KHK201A) was also analysed. Below we report the analytical uncertainties for each date. The long-term reproducibility of the U(-Th)/He ages for Durango apatite and Fish Canyon zircon in the Dalhousie University Noble Gas Laboroatory are 6.4% and 4.8%, respectively.

Three zircon grains from KH03 yielded dates that range between 2.3 ± 0.01 Ma and 3.2 ± 0.02 Ma (Supp. Table 5). Three apatite grains from the same sample yield older ages: 11.0 ± 0.04 Ma, 16.7 ± 0.06 Ma and 11.0 ± 0.05 Ma (Supp. Table 5).

Three zircon grains from the specimen yielded dates of 3.10 ± 0.02 Ma, 2.70 ± 0.01 Ma, and 2.50 ± 0.01 Ma (Supp. Table 5). No suitable apatite was separated from specimen KH12.

Analysis of 5 zircon grains from specimen KHKL01B returned dates of 6.30 ± 0.03 Ma, 6.70 ± 0.03 Ma, 7.90 ± 0.04 Ma, 9.10 ± 0.05 Ma and 10.50 ± 0.04 Ma. Anomalously high Ue, Th, ^{147}Sm and Th/U for the oldest date indicates that it may be from a partially reset/inherited grain (Supp. Table 5) and as such it is not considered further. Apatite grains from the same specimen yield dates of 2.30 ± 0.01 Ma, 9.00 ± 0.04 Ma, and 2.80 ± 0.01 Ma.

Finally, 5 zircon grains were analysed from KHK201A yielding dates of 5.40 ± 0.03 Ma, 6.60 ± 0.03 Ma, 6.90 ± 0.04 Ma, 7.50 ± 0.03 Ma and 9.00 ± 0.05 Ma. Anomalously high Ue, Th, ^{147}Sm and Th/U for the ~ 7.5 Ma grain indicates it may be a contaminant and as such is not considered further (Supp. Table 5). Three apatite dates from the same specimen indicate ages of 195.90 ± 0.85 Ma, 21.90 ± 0.09 Ma, and 4.90 ± 0.02 Ma. The first two dates are older than the youngest monazite crystallization population for the same specimen. As such, they are interpreted to be not geologically meaningful and are not considered further.

5. Discussion

5.1. *U-Th/Pb Geochronology*

Uranium(-Th)/Pb geochronology of zircon, monazite and xenotime outline distinct pulses of anatexis and crystallization. Plotting the weighted mean age of the youngest discernible population versus median Cenozoic age of the specimen can provide an indication of inheritance in individual specimens (Figure 14; Cottle *et al.* 2019). Most specimens plot away from the 1:1 line, indicating significant inheritance. The main inherited components in each specimen are interpreted to define the older age peaks of ~24-25 Ma. These dates likely reflect mineral growth (metamorphism?) within the source region from which the anatexite that formed the leucogranite was extracted (e.g. Cottle *et al.* 2018).

The older magmatic pulse is generally recorded in monazite, xenotime and zircon from 4 leucogranite specimens (KHKL01B, KHK200, KHK201A, KHK201B) interpreted to be associated with the Nuptse pluton. Jessup *et al.* (2008) reported the results of 8 analyses on 4 monazite grains from a medium-grained leucogranite interpreted to be an isolated portion of the Nuptse pluton along the ridge to the north of the village of Chukhung. Those monazite analyses define a weighted mean ^{208}Pb/^{232}Th age of 23.6 ± 0.7 Ma (MSWD = 1.1, n = 6). The results of Jessup *et al.* (2008) overlap with the older population of

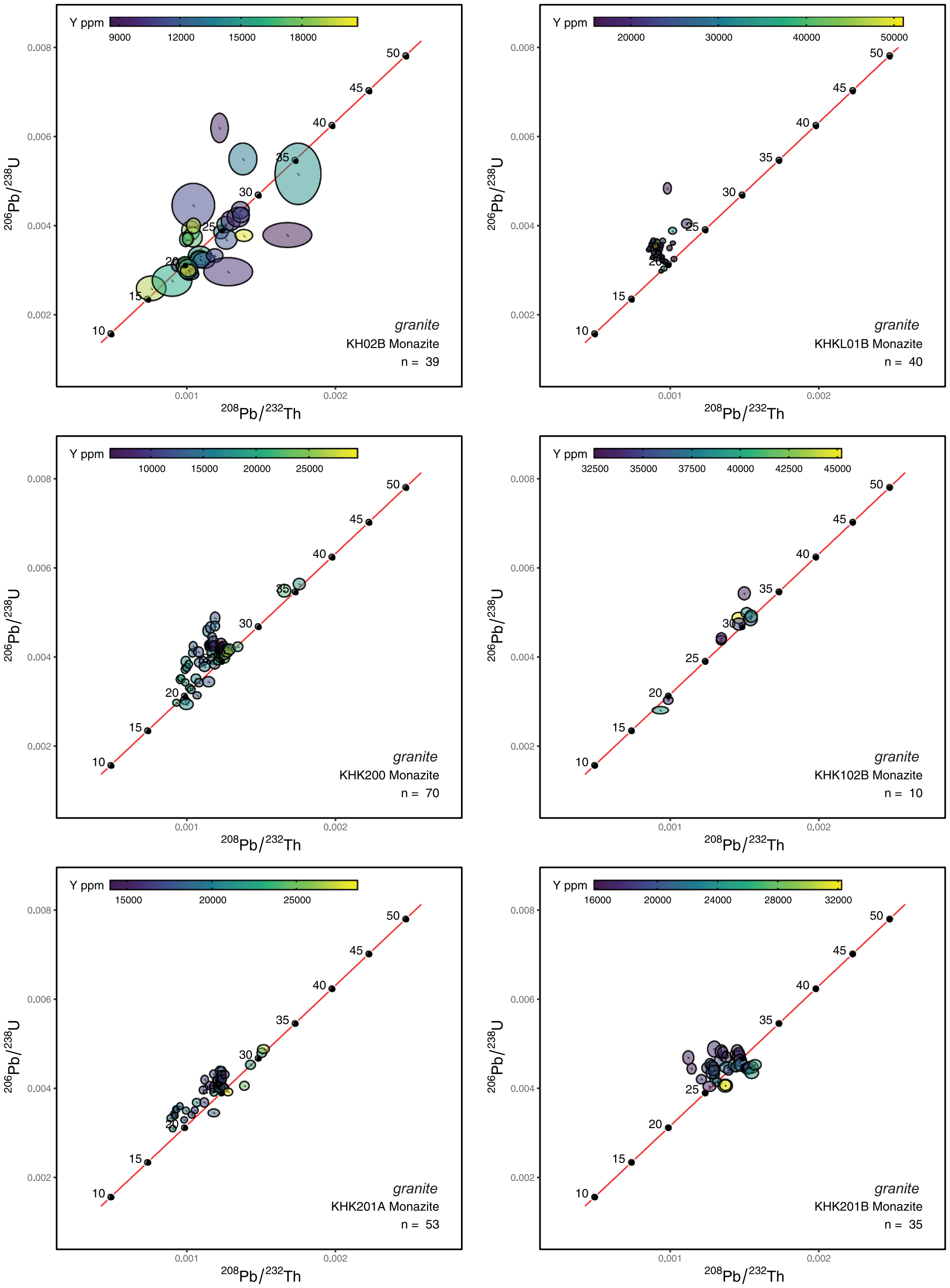

Figure 10. $^{206}Pb/^{238}U$ vs $^{208}Pb/^{232}Th$ concordia plots of monazite data. Ellipses coloured according to measured Y ppm. Plots generated using the ChrontouR package for the open R platform (Larson 2020).

the Nuptse pluton reported in the present study. The lack of a younger component in that study may reflect the amount of material analysed, as both age populations were not necessarily well represented in each specimen analysed as part of this work.

The younger, ca. 17 Ma zircon age data from leucogranite specimens all contain cm-scale skeletal tourmaline. The similarity in mineral texture, geochemistry and geochronology in these specimens (KH03, KH11, KH12, KHK101B) is consistent with them comprising a 10s of kilometre-scale sill or sill network that extends across the Khumbu as originally suggested by Searle (1999b).

Ti-in-zircon thermometry and zirconium saturation thermometry can be used to extract information about the temperature of zircon crystallization and magma generation, respectively (Watson and Harrison 1983; Ferry and Watson 2007). Rutile was not observed in any of the specimens analysed and as such the Ti-in-zircon temperatures are regarded as

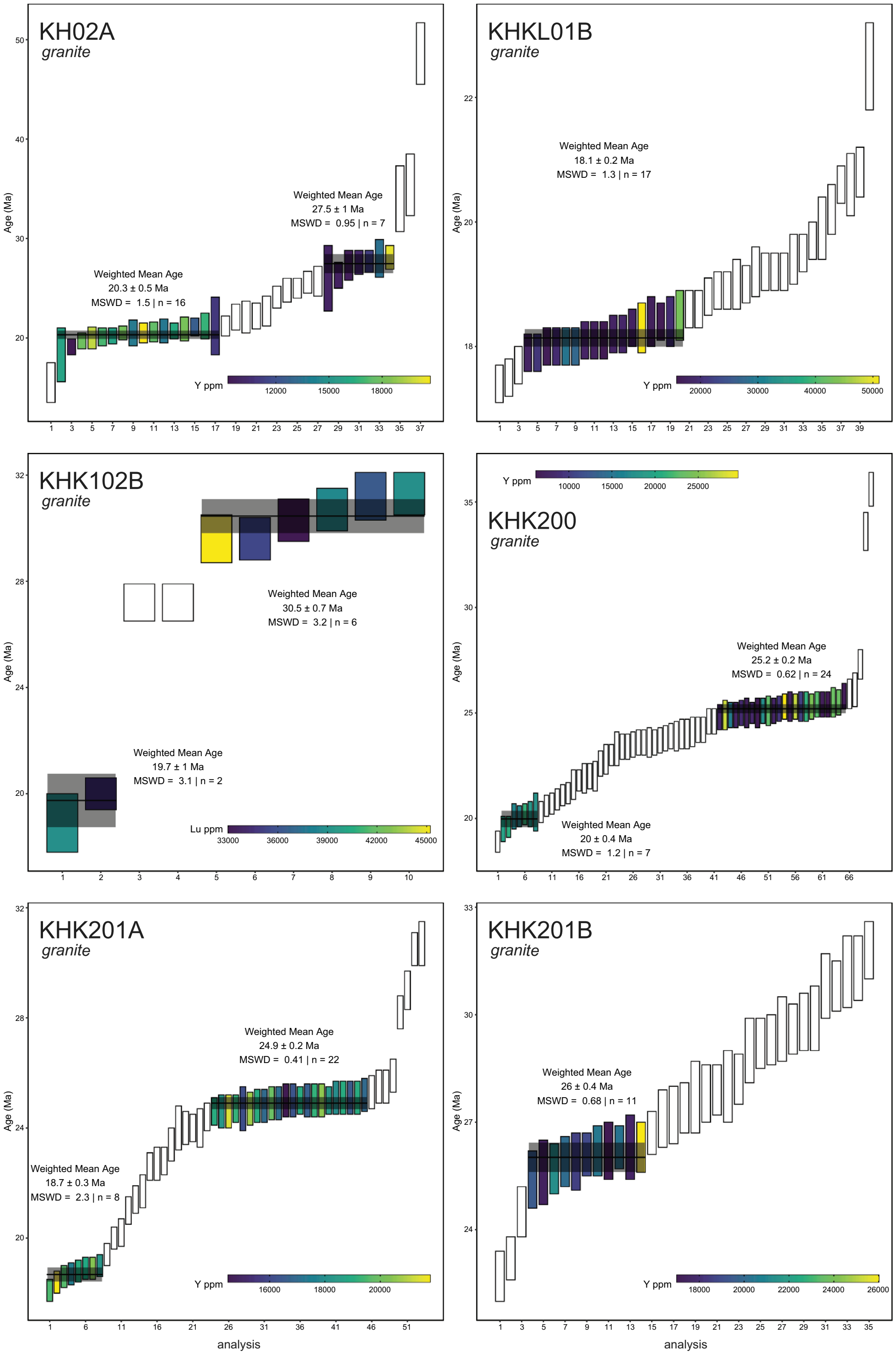

Figure 11. $^{208}Pb/^{232}Th$ monazite dates with weighted mean ages of identifiable populations shown. Plots generated using the ChrontouR package for the open R platform (Larson 2020).

minimums. These minimums range from 624 ± 32 °C in KHK201A to 710 ± 4 °C in KHK101B (Figure 9). Those temperatures generally overlap with zirconium saturation thermometry for the same rocks (Figure 9). The zirconium saturation temperatures are considered maximums as all specimens dated have inherited zircon components and, therefore, the leucogranites are likely over-saturated with respect to zirconium (e.g. Hanchar and Watson 2003).

Combining the minimum and maximum temperature estimates indicates crystallization temperatures between ~645 °C and 690 °C for specimens associated

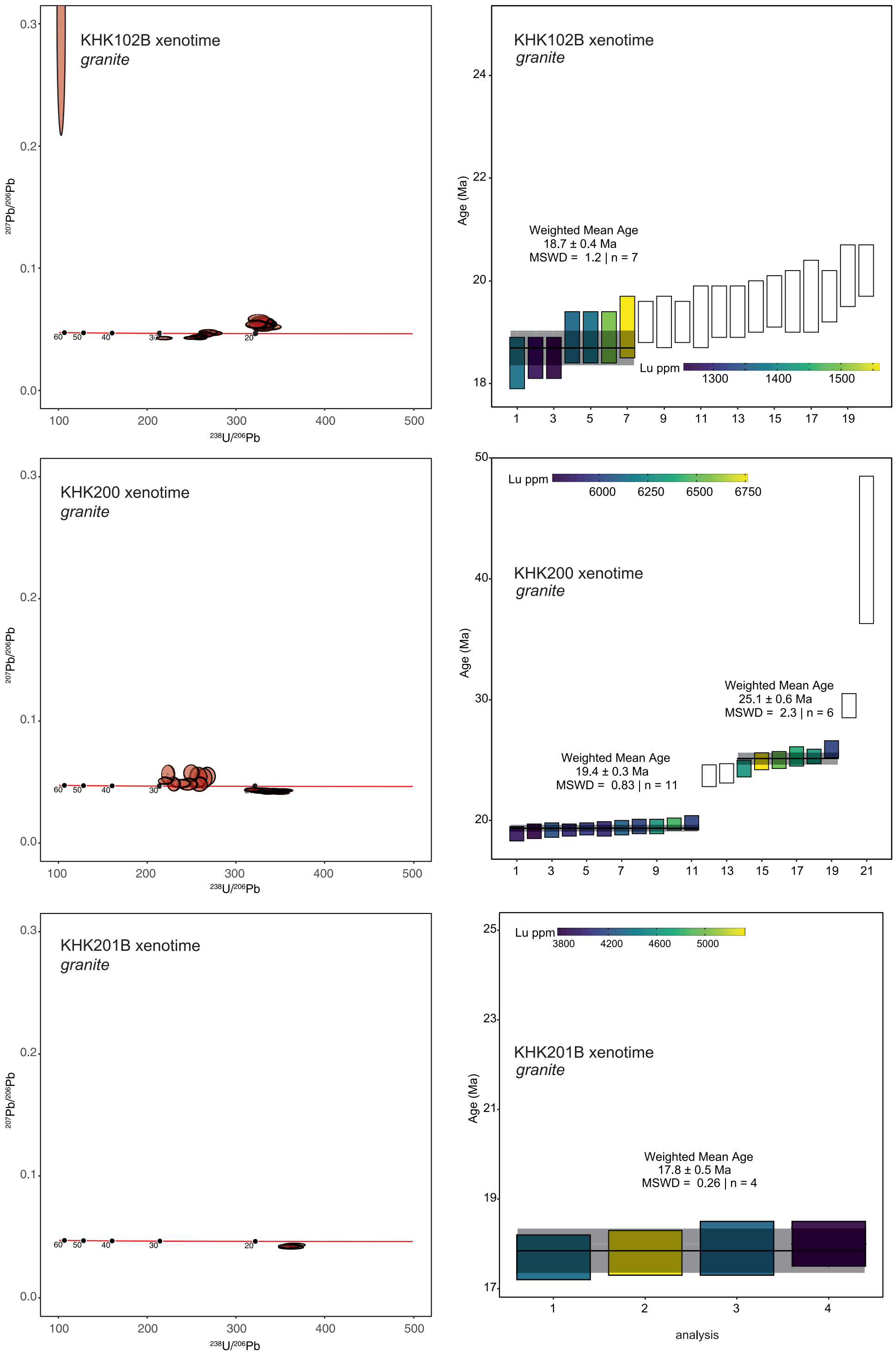

Figure 12. ^{207}Pb/^{206}Pb versus ^{238}U/ ^{206}Pb Tera-Wasserburg concordia plots of xenotime data with associated ^{207}Pb corrected (following Stacey and Kramers 1975) ^{206}Pb/^{238}U date plots with weighted means of identifiable populations marked. Plots generated using the ChrontouR package for the open R platform (Larson 2020).

with the Nuptse granite (KHK201A and KHK201B) with a final crystallization age of ca. 19 Ma and between ~710 °C and 722 °C for KHK101B, one of the specimens characterized by large, skeletal tourmaline, with a final crystallization age of ca 17 Ma. While more, detailed data are required to draw meaningful conclusions, the results presented herein are consistent with pulsed magmatism and leucogranites with younger minimum crystallization ages forming at higher temperatures.

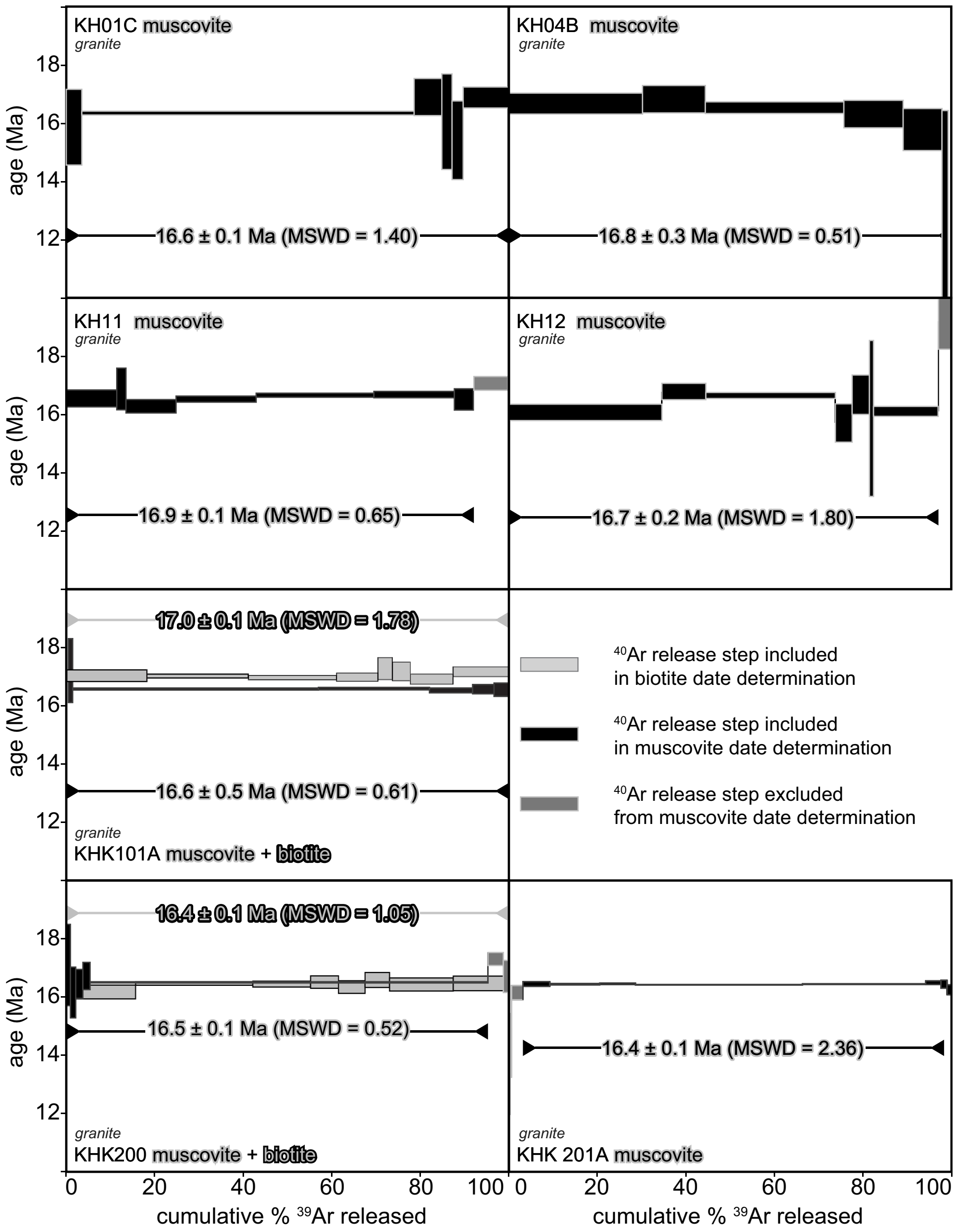

Figure 13. ^{40}Ar/^{39}Ar age spectra plots for muscovite and biotite analysed.

5.2. ^{40}Ar/^{39}Ar Thermochronology

The present work reports nearly identical ^{40}Ar/^{39}Ar dates from across the Khumbu (Figures 1; 13). When combined, 6 of 7 muscovite ^{40}Ar/^{39}Ar dates yield a weighted mean age of 16.5 ± 0.1 Ma with an MSWD of 3.05, which is slightly more dispersed than expected from a single population. Considering the spatial separation of the specimens, and the varying rock types, this is not unexpected.

5.2.1. Regional Comparisons

Previous geochronological work around the Everest massif was carried out by Ferrara *et al.* (1983) who reported: 1) a 4 point, whole-rock Rb/Sr isochron age of 13.7 ± 7.0 Ma from four specimens collected from a similar location to our specimens KHK201A and B. This date has a large uncertainty and consequently, is not precise enough for meaningful comparison, but overlaps with the muscovite ^{40}Ar/^{39}Ar age of 16.4 ± 01 Ma for KHK201A; and 2) whole-rock -mineral isochron Rb/Sr date of 16.5 ± 0.5 Ma from a specimen collected at the same location as our KH03 and is consistent with the mica ages we report from across the region.

Villa (1990) analysed, using the K/Ar method, mica in the same specimens studied by Ferrara *et al.* (1983). Biotite date of 15.9 ± 0.4 and 15.4 ± 0.4 Ma and muscovite dates of 15.7 ± 0.4 and 15.3 ± 0.4 Ma were reported for specimens collected near the toes of the Lhotse-Nup and

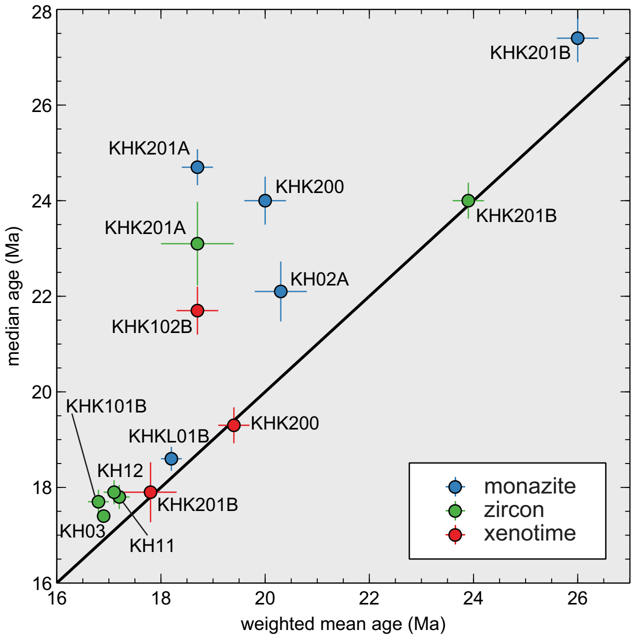

Figure 14. Median age versus weighted mean age plot of the various specimens analysed in this study. Specimens that plot above the 1:1 line have an inherited component (see Cottle *et al.* 2019).

Lhotse glaciers, respectively (Figure 1). These dates are similar to the results presented herein and any apparent differences are attributed to differences in the methods (single crystal for ^{40}Ar/^{39}Ar vs mg sized aliquots for K-Ar). The same issues around mixed aliquots and methodological differences preclude incorporation of biotite K-Ar dates from metamorphic rocks and leucogranites in the Khumbu region published by Krummenacher *et al.* (1978), which ranged widely from >47 Ma near Everest base camp to as young as 16.0 ± 0.9 Ma from just south of the village of Pangboche.

Further ^{40}Ar/^{39}Ar and Rb/Sr data from the region comes from above the Lhotse (Sakai *et al.* 2005) and Qomolangma (Corthouts *et al.* 2016) detachments. These studies outline late Eocene to late Oligocene muscovite Rb/Sr and ^{40}Ar/^{39}Ar dates from the Yellow Band (Figure 1) and a late Oligocene to early Miocene stair-stepping muscovite ^{40}Ar/^{39}Ar spectrum from just above the Qomolangma detachment. These data are generally older than that quantified herein, consistent with their positions in the hanging walls of normal-sense structures.

Finally, Viskupic *et al.* (2005) reported a series of biotite ^{40}Ar/^{39}Ar dates from just north of the town of Gokyo (Figure 1). Unfortunately, like many such dates from the Himalaya (e.g. Stübner *et al.* 2017), nearly all of the data suffered from issues related to excess Ar and were interpreted as unreliable.

5.3. *U(-Th)/He Thermochronology*

Analysis of both apatite and zircon was carried out for three specimens. In KH03, two apatite grains yield an average age of ~ 11 Ma, which is significantly older than the ~2.6 Ma average age of three zircon grains. Specimen KHK201A yielded only one meaningful apatite date (see results section) ca. 4.9 Ma, which is younger than its average zircon age of ca. 7 Ma. The U(-Th)/He data from KHKL01B follows the same basic pattern with apatite analyses that average ca. 2.6 Ma (excluding a lone date of ca. 9 Ma) and zircon grains that yield an average age of ca. 7.5 Ma. Finally, the zircon date returned from KH12 average ca. 2.8 Ma.

Some of the zircon aliquots show a positive correlation between date and eU (where eU = U + 0.235Th in ppm; Supp. Figure 11), a proxy for radiation damage (Shuster *et al.* 2006; Guenthner *et al.* 2013), and as such should be viewed with caution. The apatite aliquots do not show the same correlation between eU and date (Supp. Figure 11). Date-eU correlations may form when grains that experienced the same thermal history are re-heated or when grains with variable eU undergo slow cooling through the partial retention zone (Guenthner *et al.* 2013). Given the monotonic ^{40}Ar/^{39}Ar dates from across the Khumbu, and the lack of significant younger leucogranite intrusion that could have caused a thermal pulse, the later explanation is favoured.

The effects of eU on age may help explain the apparent discrepancy between zircon and apatite dates in KH03, where the apatite dates are significantly older (Supp. Table 5)(Guenthner *et al.* 2013). Given the size of the U(-Th)/He dataset, the limited spatial distribution and complicating factors such as positive eU-date correlations, it is not reasonable to use these data to reconstruct temperature time paths with forward or inverse modelling approaches.

5.3.1. *Regional Comparisons*

Studies by Sakai *et al.* (2005) and Streule *et al.* (2012) report apatite fission track dates from locales that overlap with the present study area. Streule *et al.* (2012) determined the cooling histories of metamorphic rocks that crop out above/north of Pangboche and below the Lhotse detachment; apatite typically yields dates of ~ 2 to 3 Ma, while the two zircon fission track dates reported of ca 6.6 ± 0.4 and 16.3 ± 0.8 Ma are widely different. Structurally higher, at and above the Lhotse detachment on the south side of Mt. Everest, apatite fission track dates increase with elevation from ~7 Ma at 6500 m to ~ 22 Ma at 7860 m and finally ~31 Ma at 8848 m (Streule *et al.* 2012). Apatite and zircon fission track ages have also been reported from the north side of Mt. Everest, near the base of the Yellow Band (8360 m); both chronometers give dates of ~ 14.5 Ma (Sakai *et al*. 2005).

The spatial distribution of the previously published data indicates distinct cooling histories between the rocks of the metamorphic core and those within the hanging walls of the Lhotse and Qomolangma detachment faults with perhaps an overall general increase in cooling ages with elevation below the detachments (Figure 15A).

5.4. *Cooling and Exhumation of the Khumbu*

The remarkable similarity in muscovite and biotite $^{40}Ar/^{39}Ar$ dates from specimens collected across the Khumbu, regardless of the inferred crystallization age, determined by U(-Th)/Pb, indicates the leucogranites share a similar post-emplacement thermal history through Ar closure in mica. The closure temperatures of the mica analysed were calculated using the equations of Dodson (1973) with the diffusion parameters for muscovite and biotite as outlined in Harrison et al. (2009) and Grove and Harrison (1996), respectively. The cooling rates used in closure temperature calculations were determined iteratively between the last crystallization age of the most proximal specimen (the same specimen where available) and interpreted crystallization temperature (see above) and the age yielded by the mica of interest and the calculated closure temperature (initial closure temperatures were guesses based on literature data). The closure temperature and cooling rate typically converged after ~3 or 4 iterations. The temperatures calculated are summarized in Supp. Table 6 with all muscovite closure temperatures yielding an average value of 507 ± 11 °C.

Combining mica dates and closure temperatures with youngest leucogranite crystallization ages and associated temperatures indicates rapid cooling immediately after intrusion (Supp. Table 6; Figure 15B). This cooling may reflect either: 1) intrusion of the youngest leucogranites into relatively cold country rocks, likely at a high structural level, or 2) tectonically controlled exhumation.

To assess the potential of rapid cooling of young leucogranite bodies, those with skeletal tourmaline, as a consequence of conductive heat loss, we developed simple thermal models using the equations of Jaeger (1964, 1968). Given the widespread spatial distribution of the similar $^{40}Ar/^{39}Ar$ ages across different rock types with varying U(-Th)/Pb ages it appears that the country rocks were at temperatures >510 °C (Supp. Table 6) at 17 Ma, the time of intrusion of the youngest leucogranites. As such, we set the background temperature for our model at 510 °C and use a thermal diffusivity of 0.7 mm^2s^{-1} (Whittington *et al*. 2009). Finally, we approximate the geometry of the leucogranites sills as infinite tabular bodies with a thickness of 2 km (see Ama Dablam leucogranite thickness in Figure 3 of Searle 1999b) and a starting temperature of 700 °C (see discussion about intrusion temperature above). Given those conditions, the Jaeger (1964, 1968) model predicts that after 500 ka, the sill cools down to 542–540 °C. These temperatures are slightly higher than the average Ar closure temperature of 507 ± 11 °C (Supp. Table 4), however, given the

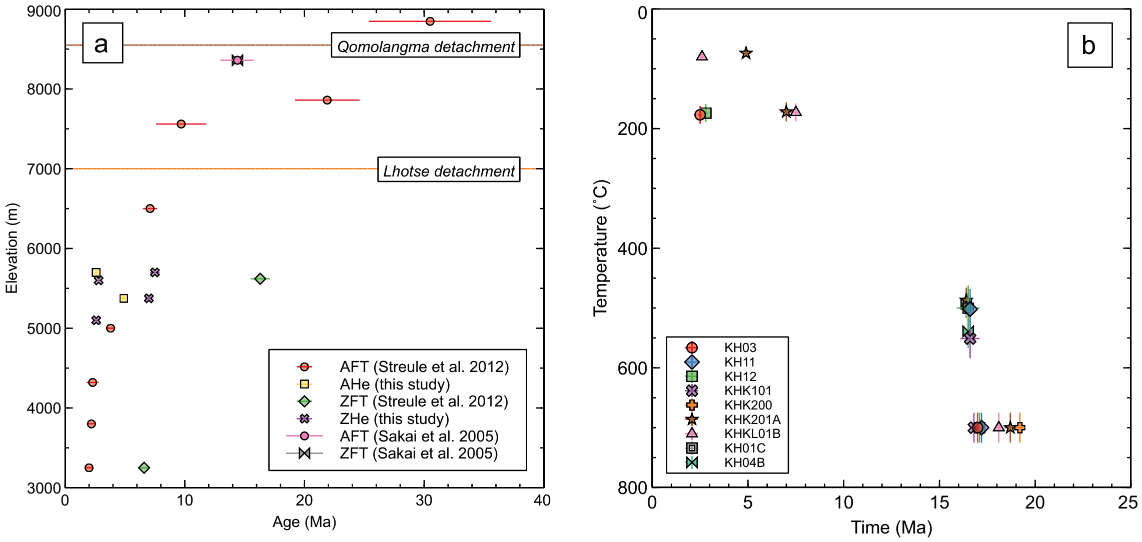

Figure 15. A) Plot of age versus sampling elevation for apatite and zircon fission track and U(-Th)/He ages reported in the present work, Streule *et al*. (2012) and Sakai *et al*. (2005). The approximate locations of the Lhotse and Qomolangma detachments are shown. B) Temperature versus time plots of data presented in the present study. See text for discussion of temperature quantification for $^{40}Ar/^{39}Ar$ and U-Th/Pb data. Closure temperatures of 170–220 °C was used for zircon U(-Th)/He, while 55–90 °C was used for apatite U (-Th)/He, covering a broad range of grain sizes, cooling rate and potential effects of radiation damage (Reiners 2005).

assumptions inherent in these simple conductive modelling and closure temperature calculations it is possible that cooling of the 17 Ma leucogranite bodies was conductive.

Beyond just the 17 Ma leucogranite bodies, the regional nature of synchronous, often rapid cooling across different rock types of varying crystallization ages may reflect large-scale tectonic processes. Past work has mapped high-angle normal sense faults, some with motion coeval with sillimanite growth (Musumeci 2002), in the central portion of the study area (Figure 1). The total displacement on these structures, however, is largely unconstrained, though it does not appear to be substantial (see Figure 3 in Hubbard *et al.* 2021). Moreover, the mapped structures do not seem to extend into the areas of the Khumbu that were sampled, potentially limiting their effect on the specimens examined, and there is no detailed information available about when movement occurred only minimum ages from thermochronology (see Musumeci 2002).

In contrast, recent work on specimens collected from the Qomolangma detachment on the Mt. Everest massif indicates that ductile movement across that normal-sense ductile shear zone occurred at 16.3 ± 5 Ma (Larson *et al.* 2020), coincident with the widespread cooling recognized herein across the region. Farther north, in the Rongbuk valley of Tibet (Figure 1), Cottle *et al.* (2015) documented ductile deformation along the same detachment at ca. 15.6 Ma that transitioned to brittle deformation shortly thereafter (<15.4 Ma). The results of that work are compatible with ca. 15.3 and 14.6 Ma synkinematic muscovite and biotite ages (Gébelin *et al.* 2017), ca. 14–17 Ma U(-Th)/He zircon ages (Orme *et al.* 2015) and rapid cooling/tectonic exhumation associated with brittle-ductile slip between ca.15.4 and 13.0 Ma (Schultz *et al.* 2017) from the same area. These geochronological datasets are compatible with tectonically driven exhumation and cooling of the Khumbu region, in the footwall of the Qomolangma detachment (Figure 16).

The lower temperature thermochronometer data from the Khumbu show that rapid cooling likely ceased prior to ca. 8 Ma, the oldest zircon U(-Th)/He ages. If a Streule *et al.* (2012) zircon fission track date of 16.3 ± 0.8 Ma from Kala Pattar, the same location as KH11, is reliable, it would extend rapid cooling through zircon fission track annealing closure, ~210 to 365 °C depending on cooling rate and amount of radiation damage (Tagami *et al.* 1998; Brandon *et al.* 1998; Rahn *et al.* 2004). Rapid cooling immediately following pluton intrusion in middle Miocene time is supported by both overlapping muscovite and biotite dates from KHK200 and KHK101A and muscovite and biotite outlining a single isochron in the Rb-Sr data of Ferrara *et al.* (1983) from near Chukhung indicating a date that overlaps with the youngest U-Pb data presented herein. Slowing of cooling/exhumation of the Khumbu after middle Miocene time, is consistent with cessation of movement along the Qomolangma detachment and a transition away from tectonic exhumation to erosion-controlled exhumation.

5.5. *Magmatic Emplacement and Rheological Implications*

The intrusion of leucogranite in the Khumbu, development of migmatites notwithstanding, appears to have occurred in at least two distinct pulses, ca. 19 and 17 Ma. Previously published U(-Th)/Pb geochronological data from the Khumbu outline age peaks at ~18, 21 and perhaps 24 Ma, though data are few. If expanded to include data from the Rongbuk and Kangshung valleys to the north and west, respectively, the younger population becomes better defined and slightly younger at 17 Ma, while the older potential populations remain. What is not clear, however, is whether the ~21 and 24 Ma populations are inherited as the similar age populations are interpreted here. Quantifying the amount of anatexite present through time is an important assessment of the rheological strength of the mid-crust as a few percent partial melt can significantly weaken rocks (Beaumont *et al.* 2004). Though more, detailed work needs to be carried out, it appears that there is little record for early Miocene age anatexis preserved in the Khumbu. Moreover, the younger melting pulse coincides temporally with movement along at least the Qomolangma detachment (timing of movement along the Lhotse detachment is not well known) perhaps indicating a genetic relationship between the normal sense structures that bound the middle crust and anatexis of the rocks structurally below (e.g. Kellett *et al.* 2019).

6. Conclusions

The new U(-Th)/Pb geochronological data presented in this work outline episodic, ca. 19 and ca 17 Ma, intrusion of the dominant leucogranite phases in the Khumbu region of Nepal. When combined with ^{40}Ar/^{39}Ar and U(-Th)/He dates from the same specimens or adjacent rocks, this new dataset demonstrates rapid cooling of the entire region at ca. 16.5 Ma, coeval with movement along the normal-sense Qomolangma detachment, followed by slower cooling. While the detailed rheological consequences of melt coalescence in the Khumbu region remain uncertain, the temporal

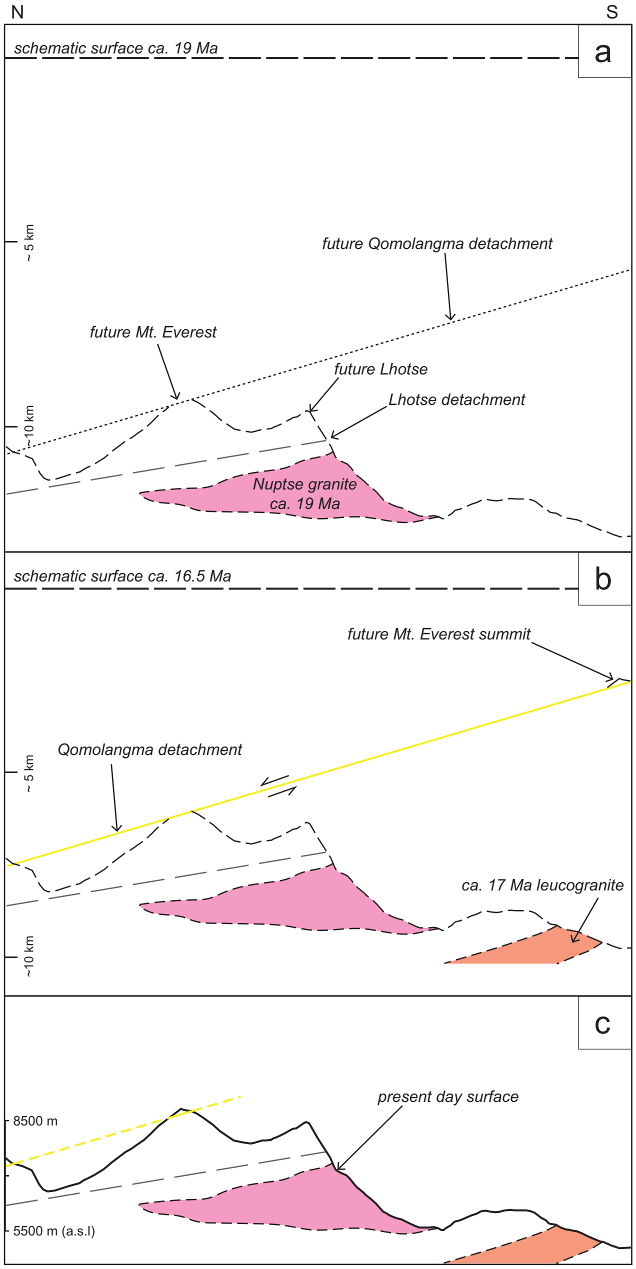

Figure 16. Schematic evolution of the Khumbu Himal. Line of topographic section is shown in Figure 1. The dashed, bold black lines in the diagrams show the relative schematic position of the surface at each interval. Note that the diagram is not drawn to vertical scale in parts A and B; it is diagrammatic. Approximate depths are marked and interpreted based on chronometer closure temperatures and a geothermal gradient of 40°C/km. A) The Khumbu at ca. 19 Ma with the Nuptse granite emplaced. Its approximate structural position is projected into the diagram. The Qomolangma detachment is not yet active. B) The ca. 17 Ma leucogranite has been emplaced and movement along the Qomolangma detachment is ongoing facilitating tectonic exhumation/cooling of the footwall. C) The present-day configuration of the Khumbu Himal.

association with major structures may indicate a kinematic relationship.

Acknowledgments

(I) Lihter, A. Brubacher and F. Gervais are thanked for their companionship and discussions in the field. Field logistics were organized by Teke Tamang and carried out by Pradap Tamang and his excellent crew. Dr. Ananta Gajurel from the Department of Geology at Tri-Chandra College is thanked for his support in obtaining the various permits required for this work. This work benefited from the comments of three anonymous reviewers and the editorial handling of R. Stern. Supplementary information and data can be accessed online: https://osf.io/6xp8q/.

Disclosure statement

No potential conflict of interest was reported by the author(s).

Funding

This work was supported by the Canada Foundation for Innovation [31301]; Natural Sciences and Engineering Research Council of Canada [RGPIN-2016-06736,RGPIN-2018-06023,RGPIN-2020-05658].

Highlights

- New U(-Th)-Pb geochronological data documents two main pulses of anatexis in the Khumbu
- ^{40}Ar/^{39}Ar geochronological data from the same specimens show rapid cooling after emplacement
- Rapid cooling coincides with movement along the South Tibetan detachment system
- U(-Th)/He geochronological data indicate slower cooling post-Ar closure in mica

References

Aleinikoff, J.N., Schenck, W.S., Plank, M.O., Srogi, L., Fanning, C.M., Kamo, S.L., and Bosbyshell, H. 2006; Deciphering igneous and metamorphic events in high-grade rocks of the Wilmington Complex, Delaware: Morphology, cathodoluminescence and backscattered electron zoning, and SHRIMP U-Pb geochronology of zircon and monazite. Geological Society of America Bulletin. 118(1–2);39–64. 10.1130/B25659.1

Annen, C., Scaillet, B., and Sparks, R.S.J. 2006; Thermal Constraints on the Emplacement Rate of a Large Intrusive Complex: The Manaslu Leucogranite, Nepal Himalaya. Journal of Petrology. 47. 71–95.

Arita, K. 1983; Origin of the inverted metamorphism of the lower Himalayas, central Nepal. Tectonophysics. 95(1–2);43–60. 10.1016/0040-1951(83)90258-5

Beaumont, C., Jamieson, R.A., Nguyen, M.H., and Medvedev, S. 2004; Crustal channel flows: 1. Numerical models with applications to the tectonics of the Himalayan-Tibetan orogen. Journal of Geophysical Research: Solid Earth. 109(B6): 10.1029/2003jb002809

Bons, P.D., Druguet, E., Hamann, I., Carreras, J., and Passchier, C. W. 2004; Apparent boudinage in dykes. Journal of Structural Geology. 26(4);625–636. 10.1016/j.jsg.2003.11.009

Bordet, P. 1961; Recherches Géologiques dan l'Himalaya du Népal, Région du Makalu. Paris: C.N.R.S. 275 p.

Brandon, M.T., Roden-Tice, M.K., and Garver, J.I. 1998; Late Cenozoic exhumation of the Cascadia accretionary wedge in the Olympic Mountains, northwest Washington State. GSA Bulletin. 110(8);985–1009. 10.1130/0016-7606(1998)110<0985:LCEOTC>2.3.CO;2

Brubacher, A.D., Larson, K.P., Cottle, J.M., Matthews, W., and Camacho, A. 2020;Progressive development of E-W extension across the Tibetan plateau: A case study of the Thakkhola graben, west-central Nepal. International Geology Review. 1–20. 10.1080/00206814.2020.1808860

Brunel, M., and Kienast, J.-R. 1986; Étude pétro-structurale des chevauchements ductiles himalayens sur la transversale de l'Everest–Makalu (Népal oriental). Canadian Journal of Earth Sciences. 23(8);1117–1137. 10.1139/e86-111

Carosi, R., Lombardo, B., Musumeci, G., and Pertusati, P.C. 1999a; Geology of the Higher Himalayan Crystallines in Khumbu Himal (Eastern Nepal). Journal of Asian Earth Sciences. 17(5–6);785–803. 10.1016/S1367-9120(99)00014-0

Carosi, R., Montomoli, C., Rubatto, D., and Visonà, D. 2013; Leucogranite intruding the South Tibetan Detachment in western Nepal: Implications for exhumation models in the Himalayas. Terra Nova. 25(6);478–489. 10.1111/ter.12062

Carosi, R., Musumeci, G., and Pertusati, P.C. 1999b. Extensional tectonics in the higher Himalayan crystallines of Khumbu Himal, eastern Nepal, in Macfarlane, A., Sorkhabi, R. B., and Quade, J. eds., Himalaya and Tibet: Mountain Roots to Mountain Tops, Geological Society of America Special Paper 328. 211-224.

Catlos, E.J., Harrison, T.M., Manning, C.E., Grove, M., Rai, S.M., Hubbard, M., and Upreti, B.N. 2002; Records of the evolution of the Himalayan orogen from in situ Th-Pb ion microprobe dating of monazite: Eastern Nepal and western Garhwal. Journal of Asian Earth Sciences. 20(5):459–479.10.1016/S1367-9120(01)00039-6

Copeland, P., Parrish, R.R., and Harrison, T.M. 1988; Identification of inherited radiogenic Pb in monazite and its implications for U–Pb systematic. Nature. 333(6175);760. 10.1038/333760a0

Corthouts, T.L., Lageson, D.R., and Shaw, C.A. 2016; Polyphase deformation, dynamic metamorphism, and metasomatism of Mount Everest's summit limestone, east central Himalaya, Nepal/Tibet. Lithosphere. 8(1);38–57. 10.1130/L473.1

Cottle, J.M., Jessup, M.J., Newell, D.L., Searle, M.P., Law, R.D., and Horstwood, M.S.A. 2007; Structural insights into the early stages of exhumation along an orogen-scale detachment: The South Tibetan Detachment System, Dzakaa Chu section, Eastern Himalaya. Journal of Structural Geology. 29 (11);1781–1797. 10.1016/j.jsg.2007.08.007

Cottle, J.M., Larson, K.P., and Yakymchuk, C. 2018;Contrasting accessory mineral behavior in minimum-temperature melts: Empirical constraints from the Himalayan metamorphic core. Lithos. 312–313. 57–71. 10.1016/j.lithos.2018.05.003

Cottle, J.M., Lederer, G., and Larson, K.P. 2019;The monazite record of pluton assembly: Mapping manaslu using petrochronology. Chemical Geology. 530. 119309. 10.1016/j.chemgeo.2019.119309

Cottle, J.M., Searle, M.P., Horstwood, M.S.A., and Waters, D.J. 2009; Timing of midcrustal metamorphism, melting, and deformation in the Mount Everest region of southern Tibet revealed by U(-Th)-Pb geochronology. The Journal of Geology. 117(6);643–664. 10.1086/605994

Cottle, J.M., Searle, M.P., Jessup, M.J., Crowley, J.L., and Law, R. D. 2015;Rongbuk re-visited: Geochronology of leucogranites in the footwall of the South Tibetan Detachment System, Everest Region, Southern Tibet. Lithos. 227. 94–106. 10.1016/j.lithos.2015.03.019

Cox, K.G., Bell, J.D., and Pankhurst, R.J. 1979; The interpretation of igneous rocks. Cox, K.G. Ed. London, England: Chapman and Hall. 450.

Dodson, M. 1973; Closure temperature in cooling geochronological and petrological systems. Contributions to Mineralogy and Petrology. 40(3);259–274. 10.1007/BF00373790

Dyck, B., Waters, D.J., St-Onge, M.R., and Searle, M.P. 2020; Muscovite dehydration melting: Reaction mechanisms, microstructures, and implications for anatexis. Journal of Metamorphic Geology. 38(1);29–52. 10.1111/jmg.12511

Faisal, S., Larson, K.P., King, J., and Cottle, J.M. 2016;Rifting, subduction and collisional records from pluton petrogenesis and geochronology in the Hindu Kush, NW Pakistan. Gondwana Research. 35. 286–304. 10.1016/j.gr.2015.05.014

Farley, K.A. 2002; (U-Th)/He dating: Techniques, calibrations, and applications. Noble Gases In Geochemistry And Cosmochemistry. 47. 819–844.

Farley, K.A., Wolf, R.A., and Silver, L.T. 1996; The effects of long alpha-stopping distances on (U Th)/He ages. Geochimica et cosmochimica acta. 60(21);4223–4229. 10.1016/S0016-7037(96)00193-7

Ferrara, G., Tonarini, S., and Lombardo, B. 1983; Rb/Sr geochronology of granites and gneisses from the Mount Everest region, Nepal Himalaya: Geologische Rundschau. Zeitschrift fur allgemeine Geologie. 72. 119–136.

Ferry, J.M., and Watson, E.B. 2007; New thermodynamic models and revised calibrations for the Ti-in-zircon and Zr-in-rutile thermometers: Contributions to mineralogy and petrology. Beitrage zur Mineralogie und Petrologie. 154. 429–437.

Frost, B.R., Barnes, C., Collins, W.J., Arculus, R.J., Ellis, D.J., and Frost, C.D. 2001; A geochemical classification for granitic rocks. Journal of Petrology. 42. 2033–2048.

Fu, J., Li, G., Wang, G., Zhang, L., Liang, W., Zhang, Z., Zhang, X., and Huang, Y. 2018; Synchronous granite intrusion and E–W extension in the Cuonadong dome, southern Tibet, China: Evidence from field observations and thermochronologic results. International Journal of Earth Sciences. 107 (6);2023–2041. 10.1007/s00531-018-1585-y

Gansser, A. 1964; Geology of the Himalayas. Interscience Publishersa division of John Wiley & Sons LtdLondon, New York, Sydney. 289 p.

Gansser, A. 1981; The geodynamic history of the Himalaya. Zagros, Hindu Kush, Himalaya: Geodynamic Evolution, Washington, D. C.: American Geophysical Union. 111–121.

Gao, L., Zeng, L.-S., Hou, K.J., Guo, C.L., Tang, S.H., and Xie, K. 2013; Episodic crustal anatexis and the formation of Paiku composite leucogranitic pluton in the Malashan Gneiss Dome, Southern Tibet. Chinese Science Bulletin = Kexue Tongbao. 58(28–29):3546–3563. 10.1007/s11434-013-5792-4

Gébelin, A., Jessup, M.J., Teyssier, C., Cosca, M.A., Law, R.D., Brunel, M., and Mulch, A. 2017; Infiltration of meteoric water in the South Tibetan Detachment (Mount Everest, Himalaya): When and why? Tectonics. 36(4);2016TC004399. 10.1002/2016TC004399

Godin, L., Grujic, D., Law, R.D., and Searle, M.P. 2006; Channel flow, ductile extrusion and exhumation in continental collision zones: An introduction. Searle, M.P., eds. Channel flow, ductile extrusion and exhumation in continental collision zones. Geological Society:London. Vol. 268. 1–23.

Godin, L., Parrish, R.R., Brown, R.L., and Hodges, K.V. 2001; Crustal thickening leading to exhumation of the Himalayan Metamorphic core of central Nepal: Insight from U-Pb Geochronology and 40 Ar/39 Ar Thermochronology. Tectonics. 20(5);729–747. 10.1029/2000TC001204

Groppo, C., Rolfo, F., and Indares, A. 2012; Partial Melting in the Higher Himalayan Crystallines of Eastern Nepal: The Effect of Decompression and Implications for the ‘Channel Flow’ Model. Journal of Petrology. 53(5);1057–1088. 10.1093/petrology/egs009

Grove, M., and Harrison, T.M., 1996, 40Ar* diffusion in Fe-rich biotite: The American Mineralogist, v. 81, p. 940–951

Guenthner, W.R., Reiners, P.W., Ketcham, R.A., Nasdala, L., and Giester, G. 2013; Helium diffusion in natural zircon: Radiation damage, anisotropy, and the interpretation of zircon (U-Th)/He thermochronology. American Journal of Science. 313 (3);145–198. 10.2475/03.2013.01

Hanchar, J.M., and Watson, E.B. 2003; Zircon Saturation Thermometry. Reviews in Mineralogy and Geochemistry. 53(1);89–112. 10.2113/0530089

Harris, N.B., and Inger, S. 1992; Trace element modelling of pelite-derived granites: Contributions to mineralogy and petrology. Beitrage zur Mineralogie und Petrologie. 110. 46–56.

Harrison, T.M., Célérier, J., Aikman, A.B., Hermann, J., and Heizler, M.T., 2009, Diffusion of 40Ar in muscovite: Geochimica et Cosmochimica Acta, v. 73, p. 1039–1051

Harrison, T.M., McKeegan, K.D., and Le Fort, P. 1995; Detection of inherited monazite in the Manaslu leucogranite by ^{208}Pb/^{232}Th ion microprobe dating: Crystallization age and tectonics implications. Earth and Planetary Sciences Letters. 133(3–4);271–282. 10.1016/0012-821X(95)00091-P

Heron, A.M. 1922; Geological Results of the Mount Everest Expedition, 1921. The Geographical Journal. 59(6);418–431. 10.2307/1780634

Hopkinson, T., Harris, N., Roberts, N.M.W., Warren, C.J., Hammond, S., Spencer, C.J., and Parrish, R.R. 2020; Evolution of the melt source during protracted crustal anatexis: An example from the Bhutan Himalaya. Geology. 48 (1);87–91. 10.1130/G47078.1

Horstwood, M.S.A. et al. 2016; Community-Derived Standards for LA - ICP - MS U-(Th-)Pb Geochronology – Uncertainty Propagation, Age Interpretation and Data Reporting. Geostandards and Geoanalytical Research. 40(3): 311–332. 10.1111/j.1751-908X.2016.00379.x

Horstwood, M.S.A., Foster, G.L., Parrish, R.R., Noble, S.R., and Nowell, G.M. 2003; Common-Pb corrected in situ U–Pb accessory mineral geochronology by LA-MC-ICP-MS:. Journal of Analytical Atomic Spectrometry. 18(8);837–846. 10.1039/B304365G

Hubbard, M. 1989; Thermobarometric constraints on the thermal history of the Main Central Thrust Zone and Tibetan Slab, eastern Nepal Himalaya. Journal of Metamorphic Geology. 7(1);19–30. 10.1111/j.1525-1314.1989.tb00572.x

Hubbard, M., Mukul, M., Gajurel, A.P., Ghosh, A., Srivastava, V., Giri, B., Seifert, N., and Mendoza, M.M. 2021; Orogenic segmentation and its role in Himalayan mountain building. Frontiers of Earth Science. 9:10.3389/feart.2021.641666

Jaeger, J.C. 1964; Thermal effects of intrusions. Reviews of Geophysics. 2(3);443. 10.1029/RG002i003p00443

Jaeger, J.C. 1968: Cooling and solidification of igneous rocks. Hess, H.H., and Poldervaart, A., eds. Basalts, the Poldervaart treatise on rocks of basaltic composition. New York-London-Sidney: Wiley. Vol. 2. 503–536.

Jessup, M.J., Cottle, J.M., Searle, M.P., Law, R.D., Newell, D.L., Tracy, R.J., and Waters, D.J. 2008; P-T-t-D paths of Everest Series schist, Nepal. Journal of Metamorphic Geology. 26 (7);717–739. 10.1111/j.1525-1314.2008.00784.x

Jochum, K.P., Nohl, U., and Herwig, K. 2005; GeoReM: A new geochemical database for reference materials and isotopic standards. Geostandards and Geoanalytical Research. 29 (3):333–338. 10.1111/j.1751-908X.2005.tb00904.x

Johnson, D.M., Hooper, P.R., and M, C.r. 1999; GeoAnalytical Lab, Washington State University. Advances in X-Ray Analysis. 41. 843–867.

Kellett, D.A., Cottle, J.M., and Larson, K.P. 2019; The South Tibetan Detachment System: History, advances, definition and future directions. Geological Society, London, Special Publications. London, Special Publications. 483(1): 377–400. 10.1144/SP483.2

Kohn, M.J. 2014; Himalayan Metamorphism and Its Tectonic Implications. Annual Review of Earth and Planetary Sciences. 42(1);381–419. 10.1146/annurev-earth-060313-055005

Kohn, M.J., Paul, S.K., and Corrie, S.L. 2010; The lower Lesser Himalayan sequence: A Paleoproterozoic arc on the northern margin of the Indian plate. Geological Society of America Bulletin. 122(3–4);323–335. 10.1130/B26587.1

Krummenacher, D., Basset, A.M., Kingery, F.A., and Layne, H.F. 1978: Metamorphism and K-Ar age determinations in eastern Nepal. Saklani, P.S., eds. Tectonic Geology of the Himalaya. New Delhi: Today and Tomorrow's Printers and Publishers, Current Trends in Geology. Vol. 1. 151–166.

Kylander-Clark, A.R.C. 2017; Petrochronology by Laser-Ablation Inductively Coupled Plasma Mass Spectrometry. Reviews in Mineralogy and Geochemistry. 83(1);183–198. 10.2138/rmg.2017.83.6

Kylander-Clark, A.R.C., Hacker, B.R., and Cottle, J.M. 2013; Laser-ablation split-stream ICP petrochronology. Chemical Geology. 345. 99–112. 10.1016/j.chemgeo.2013.02.019

Larson, K.P., 2020, ChrontouR:, doi:10.17605/OSF.IO/P46MB.

Larson, K.P., Graziani, R., Cottle, J.M., Apen, F., Corthouts, T., and Lageson, D. 2020;The structural evolution of the Qomolangma Formation, Mount Everest, Nepal. Journal of Structural Geology. 138. 104–123. 10.1016/j.jsg.2020.104123

Larson, K.P., Piercey, S., and Cottle, J. 2019; Preservation of a Paleoproterozoic rifted margin in the Himalaya: Insight from the Ulleri-Phaplu-Melung orthogneiss. Geoscience Frontiers. 10(3);873–883. 10.1016/j.gsf.2017.05.010

Lavé, J., and Avouac, J.-P. 2000; Active folding of fluvial terraces across the Siwaliks Hills, Himalayas of central Nepal. Journal Of Geophysical Research-Solid Earth. 105(B3);5735–5770. 10.1029/1999JB900292

Lederer, G.W., Cottle, J.M., Jessup, M.J., Langille, J.M., and Ahmad, T. 2013; Timescales of partial melting in the Himalayan middle crust: Insight from the Leo Pargil dome, northwest India. Contributions to Mineralogy and Petrology. Beitrage zur Mineralogie und Petrologie. 166(5): 1415–1441. 10.1007/s00410-013-0935-9

Lee, J., Hacker, B.R., and Wang, Y. 2004; Evolution of North Himalayan gneiss does: Structural and metamorphic studies in Mabja Dome, southern Tibet. Journal of Structural Geology. 26(12);2297–2316. 10.1016/j.jsg.2004.02.013

Lombardo, B., Pertusati, P., and Borghi, S. 1993; Geology and tectonomagmatic evolution of the eastern Himalaya along the Chomolungma-Makalu transect. Geological Society, London, Special Publications. London, Special Publications. 74(1): 341–355. 10.1144/GSL.SP.1993.074.01.23

Martin, A.J. 2017; A review of definitions of the Himalayan Main Central Thrust. International Journal of Earth Sciences. 106 (6);2131–2145. 10.1007/s00531-016-1419-8

Martin, A.J., Burgy, K.D., Kaufman, A.J., and Gehrels, G.E. 2011; Stratigraphic and tectonic implications of field and isotopic constraints on depositional ages of Proterozoic Lesser Himalayan rocks in central Nepal. Precambrian Research. 185(1–2);1–17. 10.1016/j.precamres.2010.11.003

McKinney, S.T., Cottle, J.M., and Lederer, G.W. 2015;Evaluating rare earth element (REE) mineralization mechanisms in Proterozoic gneiss, Music Valley, California. Geological Society of America Bulletin. B31165.1. 10.1130/B31165.1

McLennan, S.M. 2001; Relationships between the trace element composition of sedimentary rocks and upper continental crust. Geochemistry, Geophysics, Geosystems. 2(4);Paper 2000GC000109. 10.1029/2000GC000109

Musumeci, G. 2002; Sillimanite-bearing shear zones in syntectonic leucogranite: Fluid-assisted brittle–ductile deformation under amphibolite facies conditions. Journal of Structural Geology. 24(9);1491–1505. 10.1016/S0191-8141(01)00153-5

Odell, N.E. 1925; Observations on the Rocks and Glaciers of Mount Everest. The Geographical Journal. 66(4);289–313. 10.2307/1782942

Orme, D.A., Reiners, P.W., Hourigan, J.K., and Carrapa, B. 2015; Effects of inherited cores and magmatic overgrowths on zircon (U-Th)/He ages and age-eU trends from Greater Himalayan sequence rocks, Mount Everest region, Tibet. Geochemistry, Geophysics, Geosystems. 16(8);2499–2507. 10.1002/2015GC005818

Parrish, R.R., and Hodges, K.V. 1996; Isotopic constraints on the age and provenance of the Lesser and Greater Himalayan sequences, Nepalese Himalaya. Geological Society of America Bulletin. 108(7);904–911. 10.1130/0016-7606(1996)108<0904:ICOTAA>2.3.CO;2

Paton, C., Woodhead, J.D., Hellstrom, J.C., Hergt, J.M., Greig, A., and Maas, R. 2010; Improved laser ablation U-Pb zircon geochronology through robust downhole fractionation correction. Geochemistry, Geophysics, Geosystems. 11. Q0AA06.

Pearce, J.A., Harris, N.B., and Tindle, A. 1984; Trace Element Discrimination Diagrams for the Tectonic Interpretation of Granitic Rocks. Journal of Petrology. 25(4);956–983. 10.1093/petrology/25.4.956

Pearson, O.N., and DeCelles, P.G. 2005; Structural geology and regional tectonic significance of the Ramgarh thrust, Himalayan fold-thrust belt of Nepal. Tectonics. 24. TC4008.

Pêcher, A. 1989; The metamorphism in the Central Himalaya. Journal of Metamorphic Geology. 7(1);31–41. 10.1111/j.1525-1314.1989.tb00573.x

Pertusati, P.C. , pers. comm, Geological Map of the Cho Oyu, Chomlungma (Mount Everest), Makalu and Surrounding Areas (South Tibet - North-East Nepal)

Phukon, P., Sen, K., Singh, P.C., Sen, A., Srivastava, H.B., and Singhal, S. 2019;Characterizing anatexis in the Greater Himalayan Sequence (Kumaun, NW India) in terms of pressure, temperature, time and deformation. Lithos. 344–345. 22–50. 10.1016/j.lithos.2019.04.018

Pognante, U., and Benna, P. 1993; Metamorphic zonation, migmatization and leucogranites along the Everest transect of Eastern Nepal and Tibet: Record of an exhumation history. Geological Society, London, Special Publications. Special Publications. 74(1): 323–340. 10.1144/GSL.SP.1993.074.01.22

Pollard, D.D., Muller, O.H., and Dockstader, D.R. 1975; The form and growth of fingered sheet intrusions. Geological Society of America Bulletin. 86(3);351. 10.1130/0016-7606(1975)86<351:TFAGOF>2.0.CO;2

Rahn, M.K., Brandon, M.T., Batt, G.E., and Garver, J.I. 2004; A zero-damage model for fission-track annealing in zircon. The American Mineralogist. 89(4);473–484. 10.2138/am-2004-0401

Reiners, P.W. 2005; Zircon (U-Th)/He Thermochronometry. Reviews in Mineralogy and Geochemistry. 58(1);151–179. 10.2138/rmg.2005.58.6

Sakai, H., Sawada, M., Takigami, Y., Orihashi, Y., Danhara, T., Iwano, H., Kuwahara, Y., Dong, Q., Cai, H.W., and Li, J. 2005; Geology of the summit limestone of Mount Qomolangma (Everest) and cooling history of the Yellow Band under the Qomolangma detachment. Island Arc. 14(4);297–310. 10.1111/j.1440-1738.2005.00499.x

Sawyer, E.W. 1994; Melt segregation in the continental crust. Geology. 22(11);1019–1022. 10.1130/0091-7613(1994)022<1019:MSITCC>2.3.CO;2

Sawyer, E.W., Cesare, B., and Brown, M. 2011; When the Continental Crust Melts. Elements. 7(4);229–234. 10.2113/gselements.7.4.229

Scaillet, B., and Searle, M.P. 2006: Mechanisms and timescales of felsic magma segregation, ascent and emplacement in the Himalaya. Law, R.D., Searle, M.P., and Godin, L., eds. Channel Flow, Ductile Extrusion and Exhumation in Continental Collision Zones. Geological Society of London, Special Publication. Vol. 268. 293–308.

Schärer, U. 1984; The effect of inital 230Th disequilibrium on young U-Pb ages: The Makalu case, Himalaya. Earth and Planetary Sciences Letters. 67(2);191–204. 10.1016/0012-821X(84)90114-6

Schärer, U., Xu, R.-H., and Allegre, C. 1986; U-(Th)-Pb systematics and ages of Himalayan leucogranites, South Tibet. Earth and Planetary Sciences Letters. 77(1);35–48. 10.1016/0012-821X(86)90130-5

Schultz, M.H., Hodges, K.V., Ehlers, T.A., van Soest, M., and Wartho, J.-A. 2017; Thermochronologic constraints on the slip history of the South Tibetan detachment system in the Everest region. Southern Tibet: Earth and Planetary Science Letters. 459. 105–117.

Searle, M.P. 1999a; Emplacement of Himalayan leucogranites by magma injection along giant sill complexes: Examples from the Cho Oyu, Gyachung Kang and Everest leucogranites (Nepal Himalaya). Journal of Asian Earth Sciences. 17 (5–6);773–783. 10.1016/S1367-9120(99)00020-6

Searle, M.P. 1999b; Extensional and compressional faults in the Everest-Lhotse massif, Khumbu Himalaya, Nepal. Journal of the Geological Society. 156(2);227–240. 10.1144/gsjgs.156.2.0227

Searle, M.P., Law, R.D., Godin, L., Larson, K.P., Streule, M.J., Cottle, J.M., and Jessup, M.J. 2008; Defining the Himalayan Main Central Thrust in Nepal. Journal of the Geological Society. 165(2);523–534. 10.1144/0016-76492007-081

Searle, M.P., Parrish, R.R., Hodges, K.V., Hurford, A., Ayres, M.W., and Whitehouse, M.J. 1997; Shisha Pangma leucogranite, south Tibetan Himalaya: Field relations, geochemistry, age, origin, and emplacement. The Journal of Geology. 105 (3);295–317. 10.1086/515924

Searle, M.P., Parrish, R.R., Thow, A.V., Noble, S.R., Phillips, R.J., and Waters, D.J. 2010; Anatomy, age and evolution of a collisional mountain belt: The Baltoro granite batholith and Karakoram Metamorphic Complex, Pakistani Karakoram. Journal of the Geological Society. 167 (1);183–202. 10.1144/0016-76492009-043

Searle, M.P., and Rex, A.J. 1989; Thermal model for the Zanskar Himalaya. Journal of Metamorphic Geology. 7(1);127–134. 10.1111/j.1525-1314.1989.tb00579.x

Searle, M.P., Rex, A.J., Tirrul, R., Rex, D.C., Barnicoat, A., and Windley, B.F. 1989; Metamorphic, magmatic, and tectonic evolution of the central Karakoram in the Biafo-Baltoro-Hushe regions of northern Pakistan. Geological Society of America Special Papers. 232. 47–74.

Searle, M.P., Simpson, R.L., Law, R.D., Parrish, R.R., and Waters, D.J. 2003; The structural geometry, metamorphic and magmatic evolution of the Everest massif, High Himalaya of Nepal-South Tibet. Journal of the Geological Society. 160(3);345–366. 10.1144/0016-764902-126

Seeber, L., Armbruster, J.G., and Quittmeyer, R.C. 1981; Seismicity and continental subduction in the Himalayan arc. Zagros, Hindu Kush, Himalaya: Geodynamic Evolution, Washington, D. C, American Geophysical Union. 215–242.

Shuster, D.L., Flowers, R.M., and Farley, K.A. 2006; The influence of natural radiation damage on helium diffusion kinetics in apatite. Earth and Planetary Science Letters. 249(3–4);148–161. 10.1016/j.epsl.2006.07.028

Simpson, R.L., Parrish, R.R., Searle, M.P., and Waters, D.J. 2000; Two episodes of monazite crystallization during metamorphism and crustal melting in the Everest region of the Nepalese Himalaya. Geology. 28(5);403–406. 10.1130/0091-7613(2000)28<403:TEOMCD>2.0.CO;2

Spacapan, J.B., Galland, O., Leanza, H.A., and Planke, S. 2017; Igneous sill and finger emplacement mechanism in shale-dominated formations: A field study at Cuesta del Chihuido. Neuquén Basin, Argentina: Journal of the Geological Society. 174. 422–433.

Stacey, J.S., and Kramers, J.D. 1975; Approximation of terrestrial lead isotope evolution by a two-stage model. Earth and Planetary Science Letters. 26(2);207–221. 10.1016/0012-821X(75)90088-6

Streule, M.J., Carter, A., Searle, M.P., and Cottle, J.M. 2012; Constraints on brittle field exhumation of the Everest-Makalu section of the Greater Himalayan Sequence: Implications for models of crustal flow. Tectonics. 31(3);TC3010. 10.1029/2011TC003062

Streule, M.J., Searle, M.P., Waters, D.J., and Horstwood, M.S.A. 2010; Metamorphism, melting, and channel flow in the Greater Himalayan Sequence and Makalu leucogranite Constraints from thermobarometry, metamorphic modeling, and U-Pb geochronology. Tectonics. 29(5);TC5011. 10.1029/2009TC002533

Stübner, K., Warren, C., Ratschbacher, L., Sperner, B., Kleeberg, R., Pfänder, J., and Grujic, D. 2017; Anomalously old biotite 40 Ar/39 Ar ages in the NW Himalaya. Lithosphere. 9(3);366–383. 10.1130/L586.1

Sun, S.S., and McDonough, W.F. 1989: Chemical and isotopic systematics of oceanic basalts: Implications for mantle composition and processes. Saunders, A.D., and Norry, M.J., eds. Magmatism in the Ocean Basins. London: Geological Society Special Publication. Vol. 42. 313–345.

Tagami, T., Galbraith, R.F., Yamada, R., and Laslett, G.M. 1998; Revised Annealing Kinetics of Fission Tracks in Zircon and Geological Implications. van den Haute, P., and de Corte, F., eds. Advances in Fission-Track Geochronology: A selection of papers presented at the International Workshop on Fission-Track Dating, Ghent, Belgium, 1996, Dordrecht: Springer Netherlands. 99–112.

Villa, I.M. 1990; Geochronology and excess Ar geochemistry of the Lhotse Nup leucogranite. Nepal Himalaya: Journal of Volcanology and Geothermal Research. 44. 89–103.

Viskupic, K., Hodges, K.V., and Bowring, S.A. 2005; Timescales of melt generation and the thermal evolution of the Himalayan metamorphic core, Everest region, eastern Nepal: Contributions to mineralogy and petrology. Beitrage zur Mineralogie und Petrologie. 149. 1–21.

Visona, D., Carosi, R., Montomoli, C., Tiepolo, M., and Peruzzo, L. 2012;Miocene andalusite leucogranite in central-east Himalaya (Everest–Masang Kang area): Low-pressure melting during heating. Lithos. 144–145. 194–208. 10.1016/j.lithos.2012.04.012

Wager, L.R. 1933; The Mount Everest Expedition, 1933—Geological Impressions. Nature. 132(3347);976. 10.1038/132976a0

Waters, D.J. 2019; Metamorphic constraints on the tectonic evolution of the High Himalaya in Nepal: The art of the possible. Geological Society, London, Special Publications. 483(1);SP483-2018–187. 10.1144/SP483-2018-187

Watson, E.B., and Harrison, T.M. 1983; Zircon saturation revisited: Temperature and composition effects in a variety of crustal magma types. Earth and Planetary Science Letters. 64 (2);295–304. 10.1016/0012-821X(83)90211-X

Weinberg, R.F., and Searle, M.P. 1999; Volatile-assisted intrusion and autometasomatism of leucogranites in the Khumbu Himalaya. Nepal: The Journal of Geology. 107. 27–48.

Whittington, A.G., Hofmeister, A.M., and Nabelek, P.I. 2009; Temperature-dependent thermal diffusivity of the Earth's crust and implications for magmatism. Nature. 458 (7236);319–321. 10.1038/nature07818

Winchester, J.A., and Floyd, P.A. 1977;Geochemical discrimination of different magma series and their differentiation products using immobile elements. Chemical Geology. 20:325–343. 10.1016/0009-2541(77)90057-2

Zeiger, K., Gordon, S.M., Long, S.P., Kylander-Clark, A.R., Agustsson, K., and Penfold, M. 2015; Timing and conditions of metamorphism and melt crystallization in Greater Himalayan rocks, eastern and central Bhutan: Insight from U–Pb zircon and monazite geochronology and trace-element analyses: Contributions to mineralogy and petrology. Beitrage zur Mineralogie und Petrologie. 169. 1–19.

Zhang, H.-F., Harris, N.B., Parrish, R.R., Kelly, S.P., Zhang, L., Rogers, N., Argles, T.W., and King, J. 2004; Causes and consequences of protracted melting of the mid-crust exposed in the North Himalayan antiform. Earth and Planetary Sciences Letters. 228(1–2):195–212.10.1016/j.epsl.2004.09.031

Zhang, Z., Xiang, H., Dong, X., Li, W., Ding, H., Gou, Z., and Tian, Z. 2017; Oligocene HP metamorphism and anatexis of the Higher Himalayan Crystalline Sequence in Yadong region. East-central Himalaya: Gondwana Research. 41. 173–187.